

Magneto-optical investigations of phase-transition-induced band-structure changes of $\text{Pb}_{1-x}\text{Ge}_x\text{Te}$

E. Bangert

Physikalisches Institut der Universität Würzburg, D-8700 Würzburg, Federal Republic of Germany

G. Bauer and E. J. Fantner

Institut für Physik, Montanuniversität Leoben, A-8700 Leoben, Austria

H. Pascher*

Physikalisches Institut der Universität Würzburg, D-8700 Würzburg, Federal Republic of Germany

(Received 15 June 1984; revised manuscript received 2 January 1985)

The structural phase transition in semiconducting $\text{Pb}_{1-x}\text{Ge}_x\text{Te}$ from a high-temperature cubic structure to a low-temperature rhombohedral structure was studied by investigating the temperature dependence of the electronic properties. The reduction of symmetry below the phase-transition temperature T_c changes the electronic band structure. Experimentally, these changes were studied by magneto-optical intraband and interband transmission for samples with Ge content up to 1 at. % and T_c values below 50 K. Theoretically the energy-versus-momentum relationships for the T and L points of the Brillouin zone are deduced by the method of invariants and by a $\mathbf{k}\cdot\mathbf{p}$ calculation. Below T_c , the main result is the occurrence of k -linear terms described by one additional momentum matrix element. The magnetic field dependence of Landau states was derived and electric dipole intraband and interband transition elements were calculated. New transitions like spin-flip, and combined spin-flip and cyclotron-resonance harmonics appear in the low-temperature phase. Based on a linear-response formalism for the conductivity, the magnetic field dependence of the intraband transmission for far-infrared frequencies is calculated and quantitatively compared with the experimental data. The relevant band parameters were determined. An additional matrix element plays the role of a secondary order parameter evidenced by its temperature dependence. This parameter is closely related to the optical interband deformation potential which is determined for the T and L points of the Brillouin zone.

I. INTRODUCTION

Binary and pseudobinary IV-VI compounds have been the subject of numerous theoretical and experimental investigations. This research was partly stimulated by technological interest, since the narrow-band-gap IV-VI semiconducting compounds are used as infrared detectors and especially also as infrared lasers in the (4–30)- μm wavelength region. Several reviews on the electronic band-structure,^{1–4} transport,⁴ optical,^{5–7} and magneto-optical^{6,8} properties exist, with special emphasis to the lead chalcogenides.

IV-VI compounds exhibit a number of unusual properties, especially as far as their dielectric⁵ and structural properties^{7–9} are concerned. Whereas the lead compounds PbS, PbSe, and PbTe crystallize in the cubic NaCl structure (O_h), SnTe (Ref. 10) and GeTe (Ref. 11) exhibit a structural phase transition from a low-temperature rhombohedral structure (C_{3v}) to the high-temperature NaCl structure. In the pseudobinary compounds $\text{Pb}_{1-x}\text{Sn}_x\text{Te}$,⁸ $\text{Pb}_{1-x}\text{Ge}_x\text{Te}$,^{8,9,11} and $\text{Ge}_{1-x}\text{Sn}_x\text{Te}$,¹² the phase-transition temperature can be varied with composition over a wide temperature range. In particular, in $\text{Pb}_{1-x}\text{Ge}_x\text{Te}$ the critical temperature increases from 0 K for $x=0.005$ (Refs. 8 and 9) to 670 K for $x=1$.

The rhombohedral structure below the phase-transition

temperature is a distorted cubic NaCl structure (Fig. 1): (i) The two sublattices are displaced with respect to each other along one of the eight possible $\langle 111 \rangle$ directions. (ii) The angle between the axes of the unit cell differs only slightly from 90° . In GeTe, e.g., at room temperature, $\alpha=88.35^\circ$.¹¹ Pseudobinary $\text{Pb}_{1-x}\text{Ge}_x\text{Te}$ crystals which are suitable for magneto-optical and magnetotransport investigations, both in the cubic as well as in the rhombohedral phase, should exhibit a phase-transition temperature T_c not substantially higher than 80 K. For the corre-

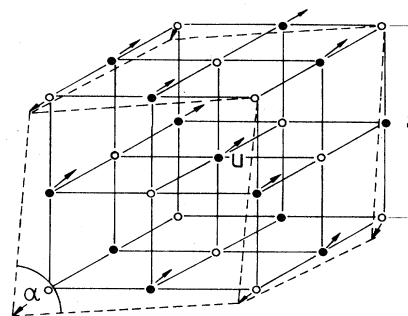


FIG. 1. Rhombohedral distortion of the cubic NaCl structure characterized by changes in the interaxial angle α , the lattice constant a , and the sublattice shift \mathbf{u} .

sponding Ge content of $x \approx 0.02$, α changes from 90° to $89^\circ 58'$ at $T = 0$ K.¹¹

An important consequence of the sublattice shift in one of the $\langle 111 \rangle$ directions, which then becomes the rhombohedral c axis, is the occurrence of a permanent electric dipole moment in the unit cell. Thus, the reduction of symmetry in these compounds below T_c induces ferroelectricity.^{13,14} Owing to the presence of free carriers, it is difficult to detect a macroscopic spontaneous polarization and any reorientation by external electric fields.

In the $\text{Pb}_{1-x}\text{Ge}_x\text{Te}$ system of interest (relatively small Ge contents), there is no indication of a discontinuity of the rhombohedral angle, which constitutes a secondary order parameter for this type of phase transition at T_c .¹¹ This is in contrast to the $\text{Sn}_{1-x}\text{Ge}_x\text{Te}$ system, which was shown to become first order for $x > 0.27$.¹²

The phase transition in the $\text{Pb}_{1-x}\text{Ge}_x\text{Te}$ system has been studied so far by various methods, which we now list.

(i) The crystal structure was investigated by x-ray diffraction.^{11,14}

(ii) Information on the lattice dynamics was obtained from inelastic-neutron-scattering (phonon dispersion) measurements.¹⁵ Raman scattering^{16,17} and far-infrared reflectivity measurements^{18,19} yielded additional evidence, namely that the structural change is connected with the softening of the zone-center transverse-optical-phonon mode ($\mathbf{q} \rightarrow 0$, \mathbf{q} denotes the phonon wave vector).

(iii) The T dependence of the lattice constant across T_c was investigated by ultrasonic velocity measurements.²⁰

(iv) Measurements of the static dielectric constant ϵ_s were performed by means of capacitance-voltage characteristics on p - n junctions²¹ and Schottky barriers on PbTe and $\text{Pb}_{1-x}\text{Ge}_x\text{Te}$.²² The data reveal that PbTe remains paraelectric down to $T = 0$ K with an extrapolated negative Curie temperature (from $\epsilon_s^{-1} \rightarrow 0$).

All experimental data on $\text{Pb}_{1-x}\text{Ge}_x\text{Te}$ with $x < 0.10$ are consistent with the occurrence of a phase transition of second order. Below T_c , these compounds, with just two atoms per unit cell, are the simplest conceivable ferroelectrics.

Since these compounds are not only ferroelectrics but also small-gap semiconductors, in addition to the methods mentioned above, typical semiconductor properties can be used to investigate the phase transition. The change of the crystal structure below T_c is accompanied by a corresponding change of the Brillouin zone (BZ) and, therefore, of the band structure (Fig. 2). Since the rhombohedral IV-VI compounds have the same crystal structure as some of the elemental group-V semiconductors such as Bi, one expects some similarities in the band structure. The four equivalent L points of the cubic BZ will be split into singlet T states (along the rhombohedral c axis) and triplet L states below T_c . In addition, the lack of inversion symmetry in the rhombohedral IV-VI compounds induces k -linear terms and lifts the Kramers degeneracy of the bands at the T and L points of the BZ. Thus, temperature-dependent measurements of semiconducting properties related to the electronic band structure should yield information on the phase transition.

Until now, an enhanced scattering of conduction elec-

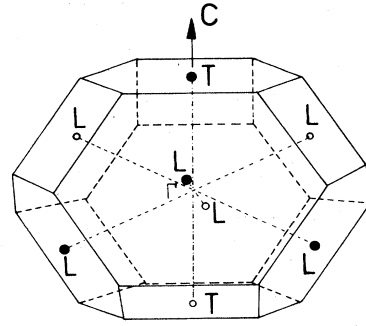


FIG. 2. Brillouin zone of rhombohedral $\text{Pb}_{1-x}\text{Ge}_x\text{Te}$ with symmetry points Γ , L , and T and the rhombohedral c axis.

trons in a temperature region around T_c and a corresponding anomaly in the T dependence of the conductivity was used by Takaoka *et al.*²³ as a very simple method to determine T_c in $\text{Pb}_{1-x}\text{Ge}_x\text{Te}$. Shubnikov-de Haas (SdH) measurements were used in Ref. 23 to obtain information on the change of the band structure below T_c . However, the experimental resolution was insufficient to distinguish between oscillation series resulting from carriers in the T and L valleys. The Fermi surface of SnTe (Ref. 24) and $\text{Pb}_{1-x}\text{Sn}_x\text{Te}$ (Ref. 25) above and below T_c has also been investigated by SdH and de Haas-van Alphen experiments. Optical absorption^{26,27,7} in $\text{Pb}_{1-x}\text{Ge}_x\text{Te}$ was performed in materials with x up to 0.1, indicating evidence for birefringence in the rhombohedral phase⁷ and differences of the energy gaps at the T and L points.

However, the most direct information on the band structure at the minimum gap at the T and L points of the BZ is obtained from magneto-optical intraband and interband experiments. Preliminary investigations were carried out in Refs. 28–30.

It is the purpose of this paper to present interband and intraband magneto-optical measurements of $\text{Pb}_{1-x}\text{Ge}_x\text{Te}$ both in the cubic and rhombohedral phase. The data are analyzed within a $\mathbf{k} \cdot \mathbf{p}$ model for the C_{3v} phase, starting with the Mitchell-Wallis³¹ scheme for PbTe, but considering the reduction of symmetry at the T and L points of the BZ.³²

In Sec. II the $\mathbf{k} \cdot \mathbf{p}$ calculation is presented and the action of the sublattice shift on the band shapes for the T and L points is described in terms of k -linear contributions to the cubic Hamiltonian. Based on this treatment, Landau levels are calculated and interband as well as intraband electric dipole matrix elements are derived quantitatively. For the comparison with magneto-optical data, this band-structure model is used to evaluate—in a linear-response formalism—the tensor of the high-frequency conductivity explicitly.

In Sec. III the experimental methods are described and in Sec. IV the results, magneto-optical interband and intraband data as a function of $T \lesssim T_c$, are presented. As a result, all band-edge parameters are derived within a $\mathbf{k} \cdot \mathbf{p}$ scheme which includes the effect of rhombohedral distortion. Information on the energy gap is directly obtained

from interband data. A complication in the analysis of the magneto-optical data arises from the occurrence of ferroelectric domains.^{8,33} The rhombohedral distortion occurs along one of the equivalent $\langle 111 \rangle$ directions. For a given orientation of \mathbf{B} with respect to the cubic crystal axes, several types of domains must be distinguished below T_c . Since the domain size is larger³³ than the cyclotron radii, no severe distortions in magneto-optical transitions occur.

In Sec. V we show that with justified simplifying assumptions only one interband matrix element is needed in addition to the cubic ones, in order to account for the main effects of the ferroelectric distortion. This additional rhombohedral matrix element plays the role of a secondary order parameter of the phase transition, since it follows closely in its temperature dependence that of the primary order parameter \mathbf{u} , the relative sublattice shift.

In Sec. V, also the optical interband deformation potential at the T and L points of the BZ is obtained from a detailed analysis of the influence of the rhombohedral distortion on the band-edge structure. The resulting values are compared with recent results from a linear combination of atomic orbitals (LCAO) calculation of the deformation potentials. Additional intraband matrix elements caused by the O_h-C_{3v} transformation change the energy gaps and the relative positions of the conduction- and valence-band extrema at the T and L points. The conse-

quences of these shifts are discussed in comparison with shifts of the energy levels induced by strain originating from the substrate, observed earlier in PbS films.³⁴

II. THEORY

A. Band structure

The electronic band states of $\text{Pb}_{1-x}\text{Ge}_x\text{Te}$ around the T and L points of the BZ can be established most generally for arbitrary x values by the method of invariants,^{35,36} because only symmetry arguments are used by this method to determine the structure of the states. Owing to the low symmetry—at the L point the group of the \mathbf{k} vector is C_s with one reflection as the only nontrivial symmetry operation—a complicated band structure described by a large number of parameters follows from this method.^{37,38}

More distinct results can be achieved by restricting one's studies to compounds with small Ge content. The $\mathbf{k}\cdot\mathbf{p}$ perturbation calculation, which considers the cubic $\text{Pb}_{1-x}\text{Ge}_x\text{Te}$ system to be unperturbed, is then an appropriate approach to obtain the band-structure changes attendant to the phase transition. Thus, the extended two-band scheme of Mitchell and Wallis is treated as the unperturbed system.³¹ It is described as

$$\underline{H} = \begin{array}{c} \begin{array}{cccc} L_{6\alpha}^- & L_{6\beta}^- & L_{6\alpha}^+ & L_{6\beta}^+ \end{array} \\ \left(\begin{array}{cccc} A(k_x^2 + k_y^2) + Bk_z^2 & 0 & -iQk_z & iL(k_x - ik_y) \\ 0 & A(k_x^2 + k_y^2) + Bk_z^2 & -iL(k_x + ik_y) & -iQk_z \\ iQk_z & iL(k_x - ik_y) & C(k_x^2 + k_y^2) + Dk_z^2 - E_G & 0 \\ -iL(k_x + ik_y) & iQk_z & 0 & C(k_x^2 + k_y^2) + Dk_z^2 - E_G \end{array} \right) \end{array} \quad (1)$$

with $L_{6\alpha, \beta}^-$ as conduction- and $L_{6\alpha, \beta}^+$ as valence-band-edge functions, and the band parameters A , B , C , D , L , Q , and E_G suitable for the cubic phase. k_z is parallel to one of the four equivalent $\langle 111 \rangle$ axes.

The difference between the lattice periodic potential above and below the phase transition is denoted by $V'(\mathbf{r})$. It is assumed that V' consists of two contributions: (i) the relative shift of both sublattices along the $[111]$ direction, which is an optical-type deformation of the cubic lattice, and (ii) the rhombohedral distortion of the cubic cell (rhombohedral angle $< 90^\circ$), which corresponds to an acoustic-type deformation. Both components will therefore increase if the temperature is lowered from T_C towards 0 K due to the second-order-type phase transition. The potential $V'(\mathbf{r})$, which is of rhombohedral symmetry, destroys the inversion symmetry of the cubic phase, and causes C_{3v} symmetry at the T point and C_s symmetry at the L points. The perturbation V' leads to the following additional elements, where the Δ_i^P and δ_i^P are all real:

$$\begin{aligned} \langle L_{6\alpha}^- | V' | L_{6\alpha}^+ \rangle &= \langle L_{6\beta}^- | V' | L_{6\beta}^+ \rangle = \Delta_1^P, \\ \langle L_{6\alpha}^- | V' | L_{6\beta}^+ \rangle &= \langle L_{6\beta}^- | V' | L_{6\alpha}^+ \rangle = i\Delta_2^P, \end{aligned} \quad (2)$$

$$\begin{aligned} \langle L_{6\alpha}^- | V' | L_{6\alpha}^- \rangle &= \langle L_{6\beta}^- | V' | L_{6\beta}^- \rangle = \delta_1^P, \\ \langle L_{6\alpha}^+ | V' | L_{6\alpha}^+ \rangle &= \langle L_{6\beta}^+ | V' | L_{6\beta}^+ \rangle = \delta_2^P, \end{aligned} \quad (3)$$

where the upper index P denotes either T or L points in order to indicate that the corresponding values of $\Delta_{1,2}$ and $\delta_{1,2}$ differ, in general, at these points. In particular,

$$\Delta_2^T = 0 \quad (4)$$

holds. Then the Mitchell-Wallis matrix for $\mathbf{k}=\mathbf{0}$ reads

$$\underline{H}(\mathbf{k}=\mathbf{0}) = \begin{array}{c} \begin{array}{cccc} L_{6\alpha}^- & L_{6\beta}^- & L_{6\alpha}^+ & L_{6\beta}^+ \end{array} \\ \left(\begin{array}{cccc} \delta_1^P & 0 & \Delta_1^P & i\Delta_2^P \\ 0 & \delta_1^P & i\Delta_2^P & \Delta_1^P \\ \Delta_1^P & -i\Delta_2^P & \delta_2^P - E_G & 0 \\ -i\Delta_2^P & \Delta_1^P & 0 & \delta_2^P - E_G \end{array} \right) \end{array} \quad (5)$$

The fact that the Δ_i^P couple the odd $L_{6\alpha}^-$ conduction-band states to the even $L_{6\alpha}^+$ valence-band states leads to the concept that the Δ_i^P dominantly represent the sublattice shift

contribution to $V'(\mathbf{r})$. This is confirmed from pseudopotential band-structure calculations,³⁹ which yielded the following results: L_6^+ states are p -like around the anion and s - and d -like around the cation, whereas L_6^- states are p -like around the cation and s - and d -like around the anion. In contrast, the diagonal elements δ_i^p dominantly represent the contribution from the distortion of the cubic cell. Therefore the δ_i^p will be evaluated from the unit-cell distortion of the lattice via acoustic deformation potentials.

The eigenvalues of $\underline{H}(\mathbf{k}=0)$ of Eq. (5) are found by the unitary transformation U ,

$$\underline{U} = \begin{pmatrix} u & 0 & -v_1 & -iv_2 \\ 0 & u & -iv_2 & -v_1 \\ v_1 & -iv_2 & u & 0 \\ -iv_2 & v_1 & 0 & u \end{pmatrix},$$

where

$$\begin{aligned} u &= \cos\theta, \quad \tan\phi = \Delta_2^p/\Delta_1^p, \\ v_1 &= \sin\theta \cos\phi, \quad v_2 = \sin\theta \sin\phi, \\ \tan(2\theta) &= 2[(\Delta_1^p)^2 + (\Delta_2^p)^2]^{1/2}/(E_G - \delta_1^p - \delta_2^p), \end{aligned} \quad (6)$$

to be given by

$$\begin{aligned} E_{c,v} &= (\delta_1^p + \delta_2^p - E_G)/2 \\ &\pm [(\delta_1^p - \delta_2^p + E_G)^2/4 + (\Delta_1^p)^2 + (\Delta_2^p)^2]^{1/2}, \end{aligned} \quad (7)$$

which defines the energy gaps in the low-temperature phase:

$$\tilde{E}_G = E_c - E_v = [(\delta_1^p - \delta_2^p + E_G)^2 + 4(\Delta_1^p)^2 + 4(\Delta_2^p)^2]^{1/2}. \quad (8)$$

In order to proceed in the evaluation of the band structure in the low-temperature phase, the Mitchell-Wallis matrix for finite \mathbf{k} values including the additional elements Δ_i^p, δ_i^p is transformed by U defined in Eq. (6):

$$\tilde{\underline{H}} = \underline{U} + \underline{H}(\mathbf{k} \neq 0)\underline{U}, \quad (9)$$

which leads to the following elements of $\tilde{\underline{H}}$:

$$\begin{aligned} \tilde{H}_{11} &= A'(k_x^2 + k_y^2) + B'k_z^2 + 2uv_2Lk_x, \\ \tilde{H}_{22} &= A'(k_x^2 + k_y^2) + B'k_z^2 - 2uv_2Lk_x, \\ \tilde{H}_{33} &= C'(k_x^2 + k_y^2) + D'k_z^2 + 2uv_2Lk_x - \tilde{E}_G, \\ \tilde{H}_{44} &= C'(k_x^2 + k_y^2) + D'k_z^2 - 2uv_2Lk_x - \tilde{E}_G, \\ \tilde{H}_{12} &= -\tilde{H}_{34} = 2iuv_1Lk^- - 2uv_2Qk_z, \\ \tilde{H}_{13} &= \tilde{H}_{24} = i(1 - 2v_2^2)Qk_z - 2iv_1v_2Lk_y, \\ \tilde{H}_{14} &= i(u^2 - v_1^2)Lk^- - iv_2^2Lk^+ - 2v_1v_2Qk_z, \\ \tilde{H}_{23} &= -i(u^2 - v_1^2)Lk^+ + iv_2^2Lk^- - 2v_1v_2Qk_z, \end{aligned}$$

with

$$A' = Au^2 + C(1 - u^2), \quad C' = Cu^2 + A(1 - u^2), \quad (10)$$

$$B' = Bu^2 + D(1 - u^2), \quad D' = Du^2 + B(1 - u^2).$$

The k -linear terms, which appear in \tilde{H}_{ii} and $\tilde{H}_{12}, \tilde{H}_{34}$,

originate from the lack of inversion symmetry of the perturbation and represent the significant changes of the band shapes.

At the T point one has $v_2=0$ from Eqs. (3) and (6), and only one k -linear parameter remains:

$$S = 2uv_1L = \sin(2\theta)L \approx 2\Delta_1^T L/E_G, \quad (11)$$

where $\delta_i^T \ll E_G$ is used. Since S will be evaluated from a comparison of calculated with experimental results at various temperatures, Eq. (11) gives Δ_1^T as a function of temperature. It turns out that the maximum value of S is about $L/7$ (for Ge contents ≤ 1 at. %), so that $u=0.997$, $v_1=0.072$, and $u^2 - v_1^2=0.992$. Therefore the interband coupling elements L in \tilde{H}_{14} and Q in \tilde{H}_{13} , as well as the far-band contributions A', B', C' , and D' in \tilde{H}_{ii} , are not changed by the phase transition, and the corresponding cubic ones can be used. The four eigenvalues $E_{i=1-4}$ of Eq. (10) which describe the band shapes near the extrema are found to be

$$\begin{aligned} E_i &= [-\tilde{E}_G + (A+C)k_\perp^2 + (B+D)k_z^2]/2 \\ &+ j\{\frac{1}{4}[\tilde{E}_G + (A-C)k_\perp^2 + (B-D)k_z^2 \mp 2Sk_\perp]^2 \\ &+ L^2k_\perp^2 + Q^2k_z^2\}^{1/2}, \quad k_\perp^2 = k_x^2 + k_y^2 \end{aligned} \quad (12)$$

where for $j = +1, -1$ the conduction- and valence-band shapes are obtained, respectively.

These bands have axial symmetry. In Fig. 3 constant-energy contours in the k_x, k_z plane are plotted for the conduction band. It is seen in Fig. 4 that the band minimum is shifted away from the T point to be on a circle with radius $k_0 \approx S/(A + L^2/\tilde{E}_G)$. Furthermore, the k -linear term causes a splitting of the Fermi surfaces be-

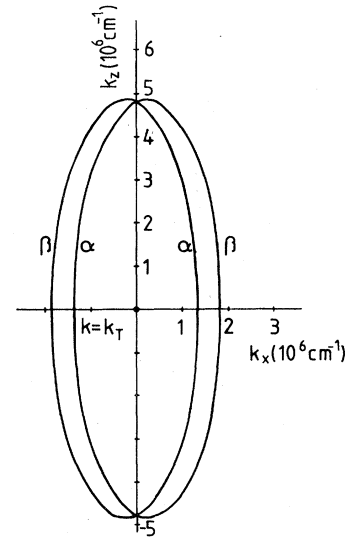


FIG. 3. Cross sections through the surfaces of constant energy ($E = E_F = 30$ meV) at the T point of the BZ ($k_z \parallel c$) with band parameters given in Table I, and $S = 6 \times 10^{-9}$ eV cm. For nonzero S , the ellipsoids of revolution found in the cubic phase are split into an inner part (α , "cigar" shaped) and an outer part (β). In the inner part each k state is twofold occupied, whereas the states outside the "cigar" are singly occupied.

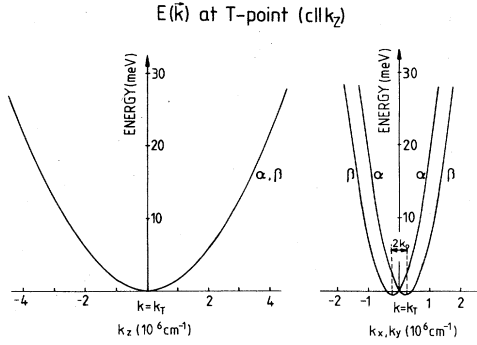


FIG. 4. $E(\mathbf{k})$ relation for the conduction band at the T point of the BZ. The shifts of the band minima by k_0 (see text) are indicated. Band parameters are given in Table I, and $S = 6 \times 10^{-9}$ eV cm.

cause the spin degeneracy is lost due to the lack of inversion symmetry. In addition, the k -linear terms produce a strong mixing of the spin components of the bands which significantly alters the optical dipole selection rules as compared to the cubic case. This is a very pronounced effect if the change of the band structure is followed beyond the phase transition, and it will be studied later in detail.

At the L point ($v_2 \neq 0$) the band structure is more complicated. Since we expect, for Δ_i^L , values which are similar to Δ_1^T , the v_i will again be about 0.07, so that contributions of second order in v_i to \tilde{H} can be neglected. Thus, there are two additional k -linear terms,

$$Rk_x = 2uv_2Lk_x, \quad Tk_z = 2uv_2Qk_z, \quad (13)$$

the magnitudes of which are related to each other by

$$LT = QR. \quad (14)$$

The band shapes near the L points derived from the Hamiltonian of Eq. (10) can be written in a form quite similar to Eq. (12), namely Sk_{\perp} on the right-hand side of Eq. (12) must be replaced by M , where

$$M = [(S^2 + R^2)k_x^2 + (Sk_y - Tk_z)^2]^{1/2}. \quad (15)$$

The term M destroys the axial symmetry of the L valleys and shifts the band extrema away from the L point by an amount $\Delta\mathbf{k}$, which has three nonzero components in general. A further approximation concerning the L -point extrema is discussed in connection with the Landau-level calculation.

It should be noticed that for materials with very small or even zero gaps, much larger S values are expected and all the approximations performed of the Hamiltonian of Eq. (10) are no longer justified.

$$\underline{H}_2 = \begin{vmatrix} p^*a^\dagger + pa & q_1a^\dagger + q_2a & 0 & 0 \\ q_1^*a + q_2^*a^\dagger & -p^*a^\dagger - pa & 0 & 0 \\ 0 & 0 & p^*a^\dagger + pa & -q_1a^\dagger - q_2a \\ 0 & 0 & -q_1^*a - q_2^*a^\dagger & -p^*a^\dagger - pa \end{vmatrix}, \quad (19)$$

where

The dominant features based on the parameters S , T , namely (i) repulsions between Landau levels of each band, and (ii) relaxed selection rules for electric dipole transitions as a consequence of spin mixing within the wave functions, are presented in the following subsections.

B. Landau levels

Adler *et al.*⁴⁰ gave a detailed description of solutions for Landau levels in a two-band model for the case of magnetic field orientations oblique to the valley symmetry axis applicable to PbTe. By a simple unitary transformation, these authors obtained exact eigenvalues and eigenfunctions if (i) the band parameters obey the following conditions,

$$A/B = C/D = L^2/Q^2, \quad L/Q = g_{\parallel}/g_{\perp}, \quad (16)$$

and (ii) there are no k -linear terms. g_{\parallel}, g_{\perp} denote the far-band contributions to the g values. It is argued by these authors that for band parameters not obeying the identities of Eq. (16), which is the case for the substances of interest, the results are not significantly falsified. Therefore, mainly the second condition, namely the k -linear terms, prevent a likewise simple Landau-level calculation in the actual case. We overcome this difficulty by the following two steps: First, we apply Adler's unitary transformation in a slightly modified version for an arbitrary oriented magnetic field \mathbf{B} ,

$$\begin{aligned} \mathbf{B} &= |\mathbf{B}|(u_1, u_2, u_3) \\ &= |\mathbf{B}|(\sin\theta \cos\phi, \sin\theta \sin\phi, \cos\theta), \end{aligned} \quad (17)$$

on the Hamiltonian of Eq. (10), and obtain

$$\underline{U}^+ \tilde{H} \underline{U} = H_1 + H_2,$$

where

$$\underline{U} = \begin{vmatrix} \underline{U}_1(\gamma, \phi) & \underline{0} \\ \underline{0} & \underline{U}_1(-\gamma, \phi) \end{vmatrix}, \quad (18)$$

$$\underline{U}_1(\gamma, \phi) = \begin{vmatrix} e^{-i\phi/2} \cos(\gamma/2) & -e^{-i\phi/2} \sin(\gamma/2) \\ e^{i\phi/2} \sin(\gamma/2) & e^{i\phi/2} \cos(\gamma/2) \end{vmatrix},$$

with

$$D_0 = (Q^2 \sin^2\theta + L^2 \cos^2\theta)^{1/2}, \quad \sin\gamma = Q \sin(\theta)/D_0.$$

u_i are the direction cosines with respect to the coordinate system, θ denotes the angle $\mathbf{x}(\mathbf{B}, z)$, and ϕ denotes the corresponding angle in the x - y plane. \underline{H}_1 stands for Adler's result (without k -linear terms) and \underline{H}_2 represents the new contributions, which are proportional to the k -linear parameters:

$$p = \{R[D_0 \cos \phi - L \cos \theta \sin \phi - 2Q^2 \sin^2 \theta \cos(\phi)/D_0] + iSQ \sin \theta\} / [s(2LD_0)^{1/2}],$$

$$q_1 = -\frac{1}{s}(TLu_1u_3/D_0 + iTu_2)(2L/D_0)^{1/2}, \quad q_2 = -\frac{1}{s}(TLu_1u_3/D_0 - iSu_3)(2L/D_0)^{1/2}, \quad s = (\hbar/eB)^{1/2}.$$

a^\dagger and a are the raising and lowering operators for the harmonic-oscillator functions. $k_B=0$ was chosen in Eq. (19), k_B being the component of \mathbf{k} parallel to the magnetic field.

From the structure of H_2 it follows that different eigenstates of H_1 are coupled by the additional part H_2 : Landau states for equal spin components are coupled by the diagonal terms, whereas states for different spin components interact via the off-diagonal terms of H_2 . This property of H_2 holds for the T valley ($R, T=0$) as well as for the L valleys ($R, T \neq 0$). Therefore the general structure of H_2 is not changed if the approximation $R, T=0$ for the L valleys is introduced. This means that we deal with a model in which the shapes of the T and L valleys are equal. Since the action from all k -linear terms, R , S , and T , are quite similar, very precise measurements would be necessary to determine these parameters separately. Indeed, our experimental data do not reveal any fine structure due to different shapes of the T and L valleys. The main advantage of this approximation is a description of the phase-transition-induced band-shape changes by a single parameter, S . Thus, our Landau-level scheme is based on the $E(\mathbf{k})$ relation, as shown in Figs. 3 and 4 for all valleys.

Because of the axial symmetry of the valleys, the Hamiltonian $H_1 + H_2$ of Eq. (18) is independent of ϕ , and H_1 is just Adler's result. For H_2 , one has

$$p^* = -p = -iSQ \sin(\theta) / [s(2LD_0)^{1/2}],$$

$$q_1 = 0, \quad q_2 = iSL \cos(\theta) / [s(2LD_0)^{1/2}].$$

θ is the angle between the valley symmetry axis and the magnetic field.

The second step for the Landau-level calculation, required to include H_2 , is a variational procedure: The eigenstates of $H_1 + H_2$ are expanded into a series of N oscillator functions, leading to a matrix representation of dimension $4N \times 4N$. A numerical diagonalization then gives the energies and wave functions of the Landau levels.

Because the k -linear parameter S is small compared to the interband coupling parameter L ($S < L/7$) in our case, a rapid convergence is the advantage of this method. To obtain eight conduction- and eight valence-band Landau levels for each spin orientation, it is sufficient to employ 40×40 matrices. Moreover, in this extended calculation the unphysical restrictions of Eq. (16) can be abandoned. The Landau states are strong mixtures of both spin components due to spin-orbit coupling already present in the

Mitchell-Wallis model, and, in addition, due to the k -linear terms. Therefore, based on the convention that the indices α, β mean spin orientation parallel and antiparallel to the valley axis, we attribute α to those states where the contribution of spin parallel to the magnetic field is dominant in the eigenfunction, and β in the opposite case. Similarly, the Landau quantum number n is attached to a state if the n th oscillator function is the dominant one. Especially for large S values and low magnetic fields, different oscillator functions or different spin components enter, with nearly equal weight, into the state functions, so that the state labels lose their conventional meaning.

The additional part H_2 produces a strong level repulsion—especially for the T valley—between states $n\alpha$ and $(n+1)\beta$, as can be seen from Eq. (19). Therefore the levels $n\alpha$ and $n\beta$ are closer in energy than in pure PbTe. This is shown in Fig. 5, together with the k_B dependence of the levels. The influence of the k -linear terms on the k_B dependence is very small in our model. In Table I the band parameters used for the numerical calculation are listed.

C. Transition matrix elements

For the interpretation of magneto-optical data the knowledge of the selection rules is indispensable and further investigation of the relative intensities is quite helpful. From a theoretical point of view, relaxed selection rules are expected as a consequence of the additional k -linear terms, which lead to extra structures in the absorption spectrum, if the Pb_{1-x}Ge_xTe sample is in its low-temperature phase. The interband absorptions show an opposite behavior, where many absorption lines—well resolved in the cubic phase—are much weaker or have disappeared completely in the rhombohedral phase. This is a direct consequence of the altered selection rules, as will be shown in the following.

The electric dipole operator $\mathbf{v} = (v_1, v_2, v_3)$, the velocity, adequate for the two-band model Hamiltonian \tilde{H} of Eq. (10), is

$$\mathbf{a} \cdot \mathbf{v} = \sum_{i=1}^3 a_i v_i = \frac{1}{\hbar} \sum_{i=1}^3 a_i \frac{\partial \tilde{H}}{\partial k_i}, \quad (20)$$

where $\mathbf{a} = (a_1, a_2, a_3)$ is the polarization unit vector of the incident radiation. Equation (20) holds for both intraband and interband transitions.

To present the dipole operator in the same Bloch-function basis used for the Landau-level calculation, Eq. (20) is transformed by Adler's unitary transformation $U(\gamma, 0)$ of Eq. (18) with the result

$$\hbar \mathbf{U}^\dagger \mathbf{a} \cdot \mathbf{v} \mathbf{U} = \hbar \mathbf{d} = \begin{vmatrix} M^* a^\dagger + Ma + SW_1 a_2 & iSa_1 + SW_3 a_2 & -iLW_1 a_1 - iQW_3 a_3 & iLW_3 a_1 + La_2 - iQW_1 a_3 \\ -iSa_1 + SW_3 a_2 & M^* a^\dagger + Ma - SW_1 a_2 & -iLW_3 a_1 + La_2 + iQW_1 a_3 & -iLW_1 a_1 - iQW_3 a_3 \\ iLW_1 a_1 + iQW_3 a_3 & iLW_3 a_1 + La_2 - iQW_1 a_3 & N^* a^\dagger + Na + SW_1 a_2 & -iSa_1 - SW_3 a_2 \\ -iLW_3 a_1 + La_2 + iQW_1 a_3 & iLW_1 a_1 + iQW_3 a_3 & iSa_1 - SW_3 a_2 & N^* a^\dagger + Na - SW_1 a_2 \end{vmatrix}, \quad (21)$$

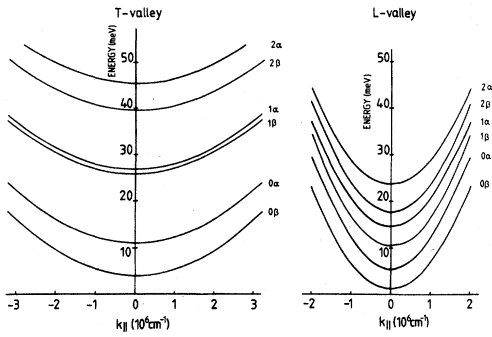


FIG. 5. Landau states for T and L valleys for $\mathbf{B}||c$, $B = 5$ T. ($S = 6 \times 10^{-9}$ eV cm).

where

$$M = \frac{2}{s} [-iAa_1(D_0/L)^{1/2} + Aa_2 \cos(\theta)(L/D_0)^{1/2} - Ba_3 \sin(\theta)(L/D_0)^{1/2}],$$

$$N = \frac{2}{s} [-iCa_1(D_0/L)^{1/2} + Ca_2 \cos(\theta)(L/D_0)^{1/2} - Da_3 \sin(\theta)(L/D_0)^{1/2}],$$

$$W_1 = Q \sin(\theta)/D_0, W_3 = L \cos(\theta)/D_0,$$

and k_B is chosen equal to zero after the differentiation. The experiments to be described use Faraday and Voigt configurations with incident radiation parallel to the $[111]$ direction.

As already mentioned, below T_c ferroelectric domains appear, which is now important to adjoin the polarization vectors \mathbf{a} to the different valleys. In the Faraday configuration, with $\mathbf{B}||\mathbf{k}||[111]$, two types of domains must be distinguished from each other [see Fig. 6(a)]. In the A domain, the c axis is parallel to the $[111]$ direction, the z axis of the coordinate system. In B domains, the L' valley is oriented with its main axis parallel to the $[111]=z$ direction and is nonequivalent to the remaining L valleys denoted as L'' . The rhombohedral c' axis is oblique to the z direction pointing toward the T' point in the B domains. From symmetry reasons, three B domains exist.

The case of the Voigt configuration with the incident radiation propagating in the $[111]$ direction is shown in Fig. 6(b). For $\mathbf{B}||[1\bar{1}0]$, three types of domains must be distinguished from each other: A, B (twofold) and C domains. Whereas the A domain is the same as in Faraday geometry, the three equivalent B domains are split in two equivalent B domains and one C domain for a given direction of the magnetic field. Table II shows the polari-

TABLE I. Sample identification, and phonon and band parameters. For the temperature-dependent quantities E_G and S , see text.

	$n\text{-Pb}_{1-x}\text{Ge}_x\text{Te}$	$n\text{-Pb}_{1-x}\text{Ge}_x\text{Te}$
Sample identification	77.4	112.3
x	0.01	0.008
n (cm^{-3})	1.8×10^{17}	8×10^{16}
$\mu(300 \text{ K})$ (cm^2/Vs)	1100	1160
d (thickness in μm)	5.46	6.73
Phonon parameters		
Cubic phase		
ϵ_∞	38	38
ω_{TO}^2 (cm^{-2})	90 (at 50 K)	90 (at 30 K)
$\epsilon_s - \epsilon_\infty$	5450	5450
Rhombohedral phase		
ω_{TO}^2 (cm^{-2})	90 (at 30 and 40 K)	90 (at 20 and 25 K)
	120 (at 20 K)	100 (at 10 K)
	150 (at 10 K)	150 (at 0 K)
	200 (at 0 K)	
$\epsilon_s - \epsilon_\infty$	5450 (at 30 and 40 K)	5450 (at 20 and 25 K)
	4080 (at 20 K)	4900 (at 10 K)
	3250 (at 10 K)	2430 (at 0 K)
	2430 (at 0 K)	
Γ (damping in cm^{-1})	2	2
Band parameters		
$A = 4.7 \times 10^{-15}$ eV cm^2	$L = 4.30 \times 10^{-8}$ eV cm	$g_{ }^c = -3.8$
$B = 0.32 \times 10^{-15}$ eV cm^2	$Q = 1.53 \times 10^{-8}$ eV cm	$g_{\perp}^c = 0$
$C = -6.79 \times 10^{-15}$ eV cm^2		$g_{ }^v = 1.89$
$D = 0$		$g_{\perp}^v = 0$

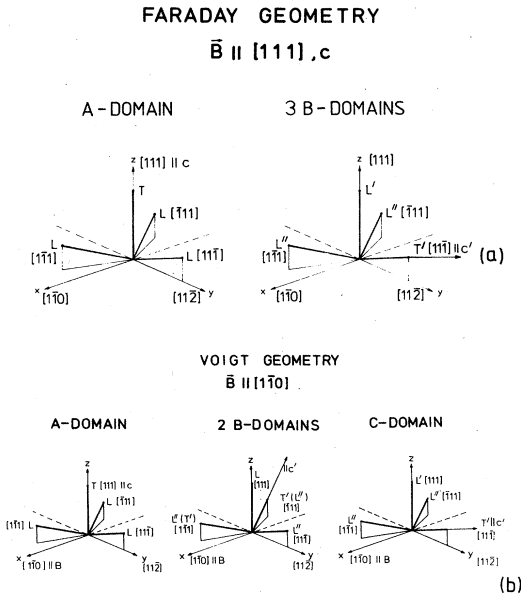


FIG. 6. (a) Schematic representation of valley symmetries and domain structure, as relevant for measurements in Faraday geometry with films grown in cubic [111] direction. In the equivalent *B* domains the *T'* and *L''* points are interchanged. (b) Same as (a), but for Voigt geometry for **B**||[110] and propagation direction of light parallel to the growth direction, [111].

zation vectors **a** and the θ values which had been inserted in the dipole operator of Eq. (21). For the Voigt configuration the two valleys with symmetry axes perpendicular to the magnetic field are not equivalent with respect to the polarization **a**||**B**. The appropriate interband matrix elements differ strongly, as can be seen from the fourth and sixth rows of the last column of Table II. No simple selection rules can be extracted from the structure of *d*, for the rhombohedral phase, because *d* is complicated by itself and, further, the Landau functions are mixtures of Adler's functions, as mentioned above. The explicit calculation of the dipole moments $\langle f | d | i \rangle$ was performed numerically, where for the final states $|f\rangle$ and initial states $|i\rangle$ the 40-dimensional eigenvectors of the numerical matrix diagonalization were introduced.

TABLE II. Polarization vectors **a** for Faraday and Voigt configurations. The valley and domain notations are those of Fig. 6. The components of **a** refer to valley inherent coordinates where the third axis coincides with the valley axis.

Valleys		a	Typical interband values for $ \langle f \mathbf{a} \cdot \mathbf{v} i \rangle ^2$ (cubic)
Faraday configuration			
<i>T</i> (<i>A</i>), <i>L'</i> (<i>B</i>)	0°	(1, ± <i>i</i> , 0)√2	8000(10 ¹² cm/s) ²
<i>L</i> (<i>A</i>), <i>L''</i> (<i>B</i>), <i>T'</i> (<i>B</i>) ⁷	70.53°	(∓1/3, 1, ± <i>i</i> (√8/3))/2	4400
Voigt configuration			
<i>T</i> (<i>A</i>), <i>L'</i> (<i>B</i>), <i>L'</i> (<i>C</i>)	90°	a B (1,0,0)	5000
		a ⊥ B (0,1,0)	4500
<i>L</i> (<i>A</i>), <i>L''</i> (<i>B</i>), <i>T'</i> (<i>C</i>)	90°	a B (1,0,0)	5000
		a ⊥ B (0, -1/3, √8/3)	900
<i>L</i> (<i>A</i>), <i>L''</i> (<i>B</i>), <i>T'</i> (<i>B</i>), <i>L''</i> (<i>C</i>)	35.26°	a B (1/√3, 0, √2/3)	1000
		a ⊥ B (-2/3, 1/√3, -√2/3)	3000

1. Magneto-optical interband absorption

For the explanation of the interband data, the dipole moments $\langle f | d | i \rangle$ were calculated considering any combination of valence-band $|i\rangle$ and conduction-band $|f\rangle$ states up to the eighth Landau level for various magnetic fields. As an example, all dipole elements squared greater than 150×10^{12} (cm/s)² for the Faraday configuration and a magnetic field strength *B* = 3 T are listed in Table III, together with those for the cubic case—without *k*-linear terms—for comparison. For the *T*, *L'* valleys additional transitions become allowed in the rhombohedral phase, but the largest elements confirm the ordinary selection rules in the left part of Table III(a). Thus, the contribution from these valleys to the absorption spectrum in the rhombohedral phase will be similar to that of the cubic phase. Table III(b) shows that the situation for the obliquely oriented valleys (*L*, *T'*, *L''*) is different. First, the dipole elements are smaller than those for the parallel oriented valleys. Furthermore, the number of transitions more or less equal to intensity is much larger in the rhombohedral than in the cubic phase. This is additionally demonstrated in the fan chart for the Faraday configuration (Fig. 7), where nearly all the allowed transitions are shown. Therefore, one would expect a contribution to the overall background absorption and, at most, a few weak structures accounting for a finite broadening of the levels.

2. Magneto-optical intraband absorption

To perform a careful analysis of the cyclotron absorption experiments, we must calculate the absorption spectrum as a function of the magnetic field strength for various frequencies and temperatures above and below *T_c*. This is indispensable because the intensities of the structures originating from different transitions depend sensitively not only on the dipole matrix elements, but also on the density of states, the occupation of the initial and final states, and, in addition, on the fact whether the resonances associated with the corresponding transitions occur in the positive or negative branch of the real part of the dielectric function. The procedure is as follows: First we calculate the conductivity $\sigma(\omega)$ within the model presented before, then the lattice contribution $\epsilon_L(\omega)$ to the dielectric

TABLE III. (a) Interband dipole elements $d_{fi}^2 = |\langle f | \mathbf{a} \cdot \mathbf{v} | i \rangle|^2$ for T, L' valleys and polarizations $\mathbf{a}^\pm = (1, \pm, i, 0)/\sqrt{2}$. ($Cn\alpha$ indicates a conduction-band state of Landau quantum number n and spin component α ; $Vn\alpha$ indicates that for a valence-band state.) d_{fi}^2 in units of 10^{12} (cm/s) 2 . d_{fi}^2 is evaluated for $B = 3$ T. (b) Interband dipole elements $d_{fi}^2 = |\langle f | \mathbf{a} \cdot \mathbf{v} | i \rangle|^2$ for L, L'', T' valleys and polarizations $\mathbf{a}^\pm = (\mp 1/3, 1, \pm i(\sqrt{8/3}))/\sqrt{2}$. [Symbols and units as in (a)]. d_{fi}^2 is evaluated for $B = 3$ T.

Without k -linear terms			(a)								
$ i\rangle$	$ f\rangle$	d_{fi}^2	$ i\rangle$	$ f\rangle$	d_{fi}^2	$ f\rangle$	d_{fi}^2				
\mathbf{a}^+											
$V0\beta$	$C0\alpha$	8248	$V0\beta$	$C0\alpha$	5846	$C1\beta$	2398				
			$V0\alpha$	$C1\alpha$	1406	$C2\beta$	510				
$V1\beta$	$C1\alpha$	7844	$V1\beta$	$C1\alpha$	3777	$C2\beta$	2185				
			$V1\alpha$	$C2\alpha$	1688	$C3\beta$	604				
$V2\beta$	$C2\alpha$	7569	$V2\beta$	$C2\alpha$	3160	$C3\beta$	2230				
			$V2\alpha$	$C3\alpha$	1836	$C4\beta$	638				
$V3\beta$	$C3\alpha$	7425	$V3\beta$	$C3\alpha$	2813	$C4\beta$	2298				
			$V3\alpha$	$C4\alpha$	1944	$C5\beta$	655				
\mathbf{a}^-											
$V0\alpha$	$C0\beta$	8242	$V0\alpha$	$C0\beta$	6228						
			$V1\beta$	$C0\beta$	2009						
$V1\alpha$	$C1\beta$	7828	$V1\alpha$	$C0\alpha$	1732	$C1\beta$	3743				
			$V2\beta$	$C0\alpha$	524	$C1\beta$	1845				
$V2\alpha$	$C2\beta$	7569	$V2\alpha$	$C1\alpha$	1951	$C2\beta$	3135				
			$V3\beta$	$C1\alpha$	622	$C2\beta$	1954				
$V3\alpha$	$C3\beta$	7420	$V3\alpha$	$C2\alpha$	2058	$C3\beta$	2796				
(b)											
Without k -linear terms			With k -linear terms:						$S = 6 \times 10^{-9}$ eV cm		
$ i\rangle$	$ f\rangle$	d_{fi}^2	$ i\rangle$	$ f\rangle$	d_{fi}^2	$ f\rangle$	d_{fi}^2	$ f\rangle$	d_{fi}^2	$ f\rangle$	d_{fi}^2
\mathbf{a}^+											
$V0\beta$	$C0\alpha$	4535	$V0\beta$	$C0\alpha$	2591	$C0\beta$	402	$C1\beta$	765	$C1\alpha$	457
$V0\alpha$	$C0\beta$	582	$V0\alpha$	$C0\alpha$	361	$C1\beta$	291	$C1\alpha$	713	$C2\beta$	233
$V1\beta$	$C1\alpha$	4395	$V1\beta$	$C1\beta$	841	$C1\alpha$	437	$C2\beta$	760	$C3\beta$	280
$V1\alpha$	$C1\beta$	566	$V1\alpha$	$C1\beta$	257	$C1\alpha$	875	$C2\beta$	892		
$V2\beta$	$C2\alpha$	4274	$V2\beta$	$C1\alpha$	236	$C2\beta$	352	$C2\alpha$	697	$C4\alpha$	560
$V2\alpha$	$C2\beta$	551	$V2\alpha$	$C1\beta$	150	$C2\beta$	667	$C3\alpha$	1200	$C4\beta$	325
$V3\beta$	$C3\alpha$	4161	$V3\beta$	$C3\alpha$	521	$C3\beta$	560	$C5\alpha$	475	$C4\beta$	934
$V3\alpha$	$C3\beta$	530	$V3\alpha$	$C3\alpha$	632	$C4\alpha$	665	$C5\alpha$	150	$C5\beta$	249
\mathbf{a}^-											
$V0\beta$	$C0\alpha$	585	$V0\beta$	$C0\beta$	327	$C1\alpha$	216				
$V0\alpha$	$C0\beta$	4531	$V0\alpha$	$C0\beta$	2593	$C0\alpha$	477				
$V1\beta$	$C1\alpha$	572	$V1\beta$	$C0\beta$	858	$C0\alpha$	200	$C1\beta$	782	$C1\alpha$	158
$V1\alpha$	$C1\beta$	4391	$V1\alpha$	$C0\beta$	354	$C0\alpha$	778	$C1\beta$	249	$C1\alpha$	885
$V2\beta$	$C2\alpha$	564	$V2\beta$	$C0\alpha$	243	$C1\alpha$	784	$C2\beta$	748		
$V2\alpha$	$C2\beta$	4261	$V2\alpha$	$C1\beta$	900	$C2\beta$	652	$C2\alpha$	567		
$V3\beta$	$C3\alpha$	558	$V3\beta$	$C1\beta$	287	$C2\beta$	885	$C3\beta$	622		
$V3\alpha$	$C3\beta$	4102	$V3\alpha$	$C2\beta$	1145	$C3\alpha$	489	$C3\beta$	428	$C5\alpha$	203

function to obtain the total dielectric function $\epsilon(\omega)$ by

$$\epsilon(\omega) = \epsilon_L(\omega) + \frac{i}{\omega\epsilon_0} \sigma(\omega). \quad (22)$$

From the refractive index $n(\omega) + ik(\omega) = \sqrt{\epsilon(\omega)}$, the transmitted power of a parallel slab is computed and compared with the original experimental recordings.⁴¹

On the basis of linear-response theory, Wallace⁴² gave explicit formulas for the frequency-dependent magnetoconductivity for a many-valley semiconductor, which were applied for PbTe in Refs. 43 and 44. Although his

work is for parabolic bands, the results are given in model-independent quantities, so that his formulas can be used with energy levels and transition matrix elements from our model. For right-circular polarization, Wallace obtained the contribution from a single valley "s," as

$$\sigma_{++}^{(s)}(\omega) = \frac{ie^2}{m\omega} [\alpha_T - \frac{1}{2}(\alpha_T - \alpha_L) \sin^2\theta] N^{(s)} + \frac{ie^2}{\omega} \sum_{k_B} \sum_{f,i} \frac{|\langle f | \mathbf{a} \cdot \mathbf{v} | i \rangle|^2 [f(E_f) - f(E_i)]}{E_f - E_i - \hbar\omega - i\hbar/\tau}, \quad (23)$$

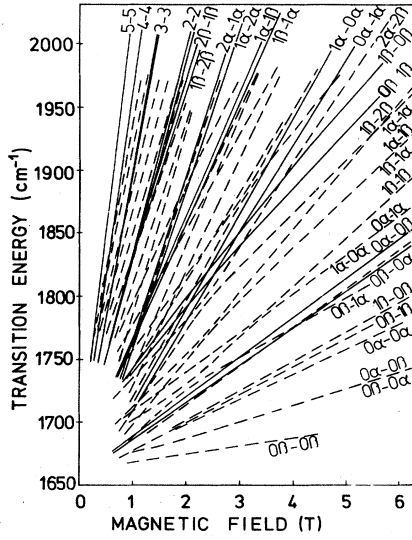


FIG. 7. Calculated transition energies as a function of magnetic field for magneto-optical interband transitions in Faraday geometry ($\mathbf{B}||c$) in the rhombohedral phase ($T=1.6$ K) with parameters as given in Table I. Solid lines, transitions within the T, L' Landau ladder system; dashed lines, transitions within the Landau ladder systems of the obliquely oriented valleys with respect to \mathbf{B} (L, L' , and T').

with ω and \mathbf{a} the frequency and polarization of the incident radiation, respectively. For the effective mass parameters α_T and α_L , we insert the values

$$\alpha_T = (2m/\hbar^2)[A + L^2/(E_G + E_F)],$$

$$\alpha_L = (2m/\hbar^2)[B + Q^2/(E_G + E_F)].$$

For carrier concentrations of the order of 10^{17} cm⁻³, the small value of the Fermi energy E_F can be neglected as compared to E_G . θ denotes the angle between the valley axis and the magnetic field direction, and $N^{(s)}$ is the carrier density in valley “ s .” The second term in Eq. (23) presents the contribution from transitions from Landau levels $|i\rangle$ to $|f\rangle$ with energies E_i and E_f , respectively. $f(E)$ denotes the Fermi function and τ a damping parameter. For the Faraday configuration, which was used in our experiments, with the magnetic field parallel to the $[111]$ direction, we must sum up the contributions from one T and three L valleys. The polarizations in these cases are already given in Table II. For the numerical calculations, we take the six lowest levels of each valley into account. The sum over the initial and final states includes any combination of these states. The value of the dipole moments squared, $d_{fi}^2 = |\langle f | \mathbf{a} \cdot \mathbf{v} | i \rangle|^2$, for $E_f > E_i$, used in this procedure, are plotted in Fig. 8 as a function of B . Indeed, many transitions—forbidden for the cubic structure—become allowed as a consequence of the level mixing by the k -linear terms. Transitions like spin flips, e.g., $T0\alpha \rightarrow T0\beta$, or combined spin-flip resonances, $L1\beta \rightarrow L2\alpha$, have dipole moments smaller than, but of the same order of magnitude as normal cyclotron resonance transitions. Furthermore, the level repulsions at about 2 and 6 T manifest themselves by breaks and kinks, where the Landau states interchange their characters. In partic-

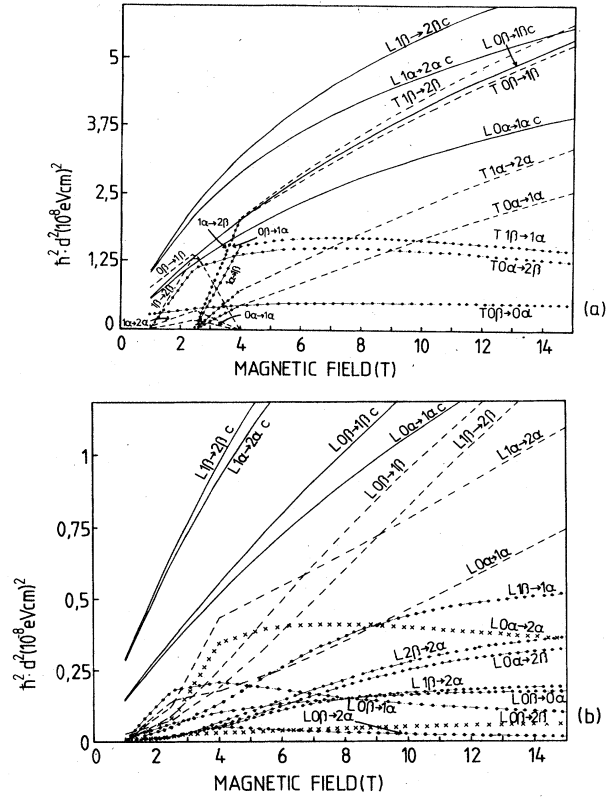


FIG. 8. (a) Intra-band transition dipole moments vs magnetic field for valleys oriented parallel to \mathbf{B} ($||[111], c$) in the Faraday configuration. Solid lines: dipole moments for the lowest cyclotron resonance transitions in the cubic phase, denoted by $L \dots c$. Dashed lines: dipole moments for cyclotron resonance transitions in the rhombohedral phase. Dotted lines: corresponding to spin-flip, combined spin-flip, and higher cyclotron resonance harmonics. ($S = 6 \times 10^{-9}$ eV cm.) (b) Same as (a), but for valleys oriented obliquely ($\approx 70^\circ$) with respect to \mathbf{B} .

ular, this occurs in the low-field region, where the levels are close to each other. Therefore the designations of the individual transitions become more or less meaningless in this field region. For comparison, the d_{fi}^2 values for the cubic case are also plotted. All elements d_{fi}^2 are evaluated for $k_B = 0$. Using the approximation of k_B -independent dipole matrix elements, the k_B summation in Eq. (23) can be performed

$$\sigma_{++}(\omega) = \sum_{s=1}^4 \frac{ie^2}{m\omega} [\alpha_T - \frac{1}{2}(\alpha_T - \alpha_L)\sin^2\theta_s] N^{(s)} + \frac{ie^2}{\omega} \sum_{s=1}^4 \sum_{f,i} \frac{d_{fi}^2 (N_f^{(s)} - N_i^{(s)})}{E_f - E_i - \hbar\omega - i\hbar/\tau}, \quad (24)$$

with $N_j^{(s)}$ as the carrier density in level j of valley “ s .” These $N_j^{(s)}$ values, which depend strongly on the magnetic field, were obtained from the calculation of the Fermi energy E_F . E_F was determined as a function of temperature and magnetic field by the constant $N = N^T + 3N^L$ condition.

Inserting an appropriate damping τ , Eq. (24) yields numerical values for the conductivity based on our band-

structure model. In the same way, $\sigma_{--}(\omega)$ for left-circular polarization was found.

For the lattice dielectric function in the cubic as well as in the rhombohedral phase, the contributions due to the high-frequency dielectric constant ϵ_∞ and the polar phonons $\epsilon_{ph}(\omega)$ must be considered,

$$\epsilon_L(\omega) = \epsilon_\infty + \epsilon_{ph}(\omega). \quad (25)$$

In the cubic phase the polar-phonon part, using a classical oscillator model, is simply given by

$$\epsilon_{ph} = \frac{(\epsilon_s - \epsilon_\infty)\omega_{TO}^2}{\omega_{TO}^2 - \omega^2 - i\omega\Gamma}, \quad (26)$$

where ω_{TO} is the TO-mode frequency and Γ is a damping parameter. Below T_c the degenerate phonon mode F_{1u} splits into an A_1 mode oscillating parallel to the c axis and a doubly-degenerate E mode oscillating perpendicular to the c axis. Therefore, ϵ_{ph} must be replaced by a tensor. However, all far-infrared reflectivity measurement failed to reveal a splitting of the TO mode for Ge contents less than 5 at.%.⁴⁵ Thus, the TO-LO-mode splitting, which is already large in the cubic phase, is much larger than the E - A_1 -mode splitting of the rhombohedral phase.⁴⁵

$$\omega_{TO}(E) \approx \omega_{TO}(A_1) \ll \omega_{LO}(E) \approx \omega_{LO}(A_1). \quad (27)$$

Since all magneto-optical experiments are carried out on samples with Ge contents less than or equal to 1 at.%, for the polar-phonon contribution, again an expression like Eq. (26) was used with phonon parameters given in Table I.

Since both contributions for right- and left-circularly-polarized light [Eq. (22)] have been derived, the total transmitted power $P(\omega, B)$ for linear-polarized radiation is the mean value of those for left- and right-circular polarization,

$$P(\omega, B) = (P_l + P_r) / 2. \quad (28)$$

For an illustration of the influence of the lattice and the free-carrier contributions on the total $\epsilon(\omega)$, a plot of ϵ as function of B is shown in Fig. 9 for $\lambda = 96.5 \mu\text{m}$.

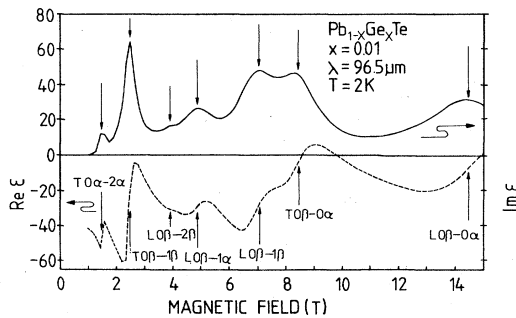


FIG. 9. Real (dashed line) and imaginary (solid line) parts of the dielectric function vs magnetic field for a photon frequency corresponding to $\lambda = 96.6 \mu\text{m}$ for the Faraday configuration, $\mathbf{B} \parallel c$. Results of model calculation (see text) for sample 77.4 with Fermi level corresponding to $n = 1.8 \times 10^{17} \text{ cm}^{-3}$. Relevant magneto-optical transitions are indicated by arrows.

III. EXPERIMENTAL DETAILS

The $\text{Pb}_{1-x}\text{Ge}_x\text{Te}$ samples were grown epitaxially on cleaved $\text{BaF}_2(111)$ substrates by a hot-wall technique.⁴⁶ The samples had typical carrier concentrations of the order of $n = 10^{17} \text{ cm}^{-3}$ and mobilities higher than $10^5 \text{ cm}^2/\text{Vs}$ at helium temperature. The sample identification and characteristic data are listed in Table I. The transition temperatures T_c were obtained from the anomaly of the T dependence of the conductivity,²³ as well as from the measured $\omega_{TO}(T)$ values¹⁹ using far-infrared reflectivity data.

Interband magneto-optical experiments were performed in transmission using as a light source a CO laser with photon energies $\hbar\omega = 195\text{--}240 \text{ meV}$. Magnetic fields up to 6 T and temperatures ranging from 1.6 to 55 K were used. The data were obtained in the Faraday geometry with $\mathbf{B} \parallel \mathbf{k} \parallel [111]$ using a CdS quarter-wave plate for producing circularly-polarized radiation. \mathbf{k} denotes the propagation vector of the laser radiation. In the Voigt geometry, both orientations $\mathbf{B} \parallel \mathbf{E}$ and $\mathbf{B} \perp \mathbf{E}$ were investigated with $\mathbf{B} \parallel [1\bar{1}0]$ [see Fig. 6(b)] and $\mathbf{k} \parallel [111]$.

Intraband magneto-optical experiments were carried out in transmission by using optically pumped molecular-gas lasers as a light source ($\lambda = 70.6, 96.5, 118, \text{ and } 163 \mu\text{m}$). The Faraday geometry $\mathbf{k} \parallel [111]$ was applied and the samples were situated in a variable-temperature insert (6–70 K) within a superconducting split coil magnet (0–7 T). Some experiments were also performed at temperatures of 2–40 K using a Bitter-type magnet up to 20 T at the High Magnetic Field Facility, Grenoble. For an analysis of the intraband data, information on the complete dielectric function is necessary, since the magneto-optical data were obtained in a frequency region between the TO- and LO-phonon-mode frequencies ω_{TO} and ω_{LO} , as well as above ω_L^+ , the coupled LO-phonon-plasmon-mode frequency. Thus, reflectivity measurements were done in the wave-number region 10–400 cm^{-1} between 4.2 and 300 K using Fourier-transform spectroscopy. Information on the frequencies $\omega_{TO}(T)$ and ω_{LO} , the phonon damping parameter Γ , $\epsilon_s(T)$, and the high-frequency dielectric constant ϵ_∞ were obtained, as well as the coupled phonon-plasmon frequency and the free-carrier damping parameter. For the analysis of the reflectivity data, multiple-reflection and interference effects within the film and substrate according to the procedure described in Ref. 41 were considered.

IV. RESULTS

A. Interband transitions

1. Faraday geometry

For about 20 CO-laser photon energies, transmission of samples 77.4 and 112.3 was measured as a function of B with temperature as the parameter. Figure 10 shows—as an example—magnetotransmission in the Faraday geometry $\mathbf{B} \parallel \mathbf{k} \parallel [111]$ for a CO-laser photon energy of 1850.9 cm^{-1} (229.4 meV) and one temperature above and several temperatures below T_c . In the cubic phase the transmission extrema are better resolved than in the

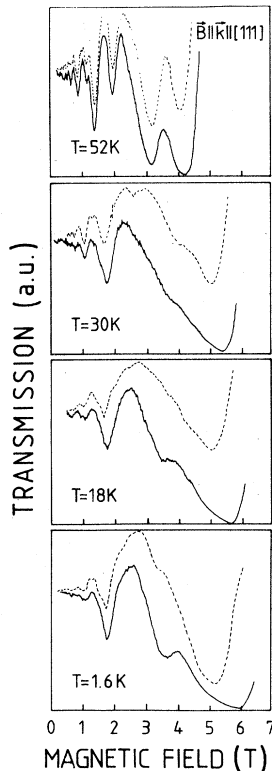


FIG. 10. Magneto-optical interband transitions vs magnetic field for various temperatures in the Faraday configuration, $\mathbf{B} \parallel [111]$ ($T=52$ K, cubic phase; other temperatures, rhombohedral phase) for sample 77.4 with σ^- (dashed lines) and σ^+ (solid lines) circularly-polarized light and a CO-laser frequency of $\bar{\nu}_L = 1605.3 \text{ cm}^{-1}$.

rhombohedral phase. In the latter case the overall transmission decreases by an order of magnitude and the modulation due to the magneto-optical interband transitions becomes weaker. Another tendency apparent from the data is the fact that interband transitions involving Landau ladder systems of the valleys oriented obliquely with respect to \mathbf{B} are much weaker below T_c than above it. The reason for this behavior is the relaxation of the principal selection rules ($n\alpha \rightarrow n\beta$, $n\beta \rightarrow n\alpha$), as pointed out in Sec. II. The oscillator strength of several closely lying transitions becomes comparable. In addition, broadening effects make it difficult to observe these transitions as transmission minima, and instead they lead to the enhanced background absorption. Since the oscillator strength of these transitions also shows a considerable dependence on B , all of these facts together makes an unambiguous identification of the transitions difficult.

The strong transmission minima are due to transitions involving the Landau ladder system of the valence and conduction band of the valley oriented parallel to \mathbf{B} —a $T(L')$ valley. In the Faraday geometry the splitting of σ^+ and σ^- transitions is readily observable, especially for transitions from $n=0(\text{VB})$ to $n=0(\text{CB})$ levels. The data indicate that the absorption due to the σ^+ transitions is

remarkably stronger than that due to the σ^- transitions. For $T < T_c$, in addition, the σ^+ transitions ($0\beta \rightarrow 0\alpha$) are not only broader, but their line shape is much more asymmetric, with an additional absorption at the low-magnetic-field side of the main minimum (see Fig. 10), especially at very low temperatures.

In Figs. 11(a)—11(d) the transmission minima are plotted as a function of B for four different temperatures: 52, 35, 18.5, and 1.6 K. The transition temperature of this sample is $T_c \approx 45$ K. The fan charts show that, in the cubic phase, $\text{Pb}_{1-x}\text{Ge}_x\text{Te}$ behaves like PbTe ,^{47,48,6} apart from the slightly larger energy gap. Below T_c , for a Ge content of about 1 at. %, there is not much variation of the apparent energy gap with temperature. However, the splitting between σ^+ - and σ^- -transition minima is much larger and, astonishingly, the extrapolation of these minima towards $B=0$ does not lead to the same energy gap. In particular, the $0\alpha \rightarrow 0\beta$ and $0\beta \rightarrow 0\alpha$ transmission minima extrapolate to different gaps, the splitting of which increases with decreasing temperature, as can be seen from a comparison of Figs. 11(a)—11(d).

These prominent features in the interband transmission fan chart originate from the Landau ladder systems of the conduction band (CB) and valence band (VB) of valleys oriented parallel to the surface normal and thus parallel to the applied field. The increase in splitting of these $0\alpha \rightarrow 0\beta$ (σ^-) and $0\beta \rightarrow 0\alpha$ (σ^+) transitions has several origins: (i) The second-order phase transition leads to a T dependence of the additional “rhombohedral” matrix elements in the matrix Hamiltonian of Eq. (10). This causes an increase of the energetic difference between σ^+ and σ^- transitions, with decreasing T and increasing B . (ii) The Fermi energy E_F lies within the conduction band in our samples, and thus a Burstein-Moss shift, however modified by the density of states in the quantizing magnetic field, occurs. The line shape and thus the position of the transmission minima do not only depend on the $E(k_B)$ dependence of the Landau levels and the magnetic-field-dependent Fermi energy, but also on the broadening of the combined density of states. In the $0 \rightarrow 0$ transitions the occupation effects will shift both the σ^+ as well as the σ^- transition for a given photon energy to smaller magnetic fields. Since the lowest-conduction-band state is a 0β state and the highest-valence-band state also a 0β state, the transitions for σ^+ -circularly-polarized radiation will be shifted by a smaller amount than the σ^- -induced transition. The k_B values in the VB and CB involved in the interband absorption process are smaller for the σ^+ ($0\beta \rightarrow 0\alpha$) than for the σ^- ($0\alpha \rightarrow 0\beta$) transitions, when E_F lies within the CB. Thus the extrapolation of the $0 \rightarrow 0$ transitions towards $B=0$ does not yield the proper energy gap but an apparent one with a higher energy. The $1 \rightarrow 1$, $2 \rightarrow 2$, etc. interband transitions are not affected by the blocking of final states for $B > 1$ and 0.5 T, respectively, and thus an extrapolation toward $B=0$ of the transition energies leads to E_G .

For the interband transitions in the cubic structure, the transition matrix elements of the valleys oriented parallel to \mathbf{B} are stronger but of the same order of magnitude as the matrix element for the obliquely oriented valleys (see Table III). In the rhombohedral phase, however, the tran-

sitions involving T Landau ladders are *much* stronger than the corresponding L Landau ladder transitions (see Table III). In addition, for the T Landau ladders, the expected selection rules for the Faraday geometry σ^- , $n\alpha \rightarrow n\beta$, and σ^+ , $n\beta \rightarrow n\alpha$, still hold. In contrast, for the L Landau ladder transitions, the usual selection rules have transition matrix elements which are comparable or even smaller than the quite unusual ones, as shown in Table III. Thus the distinct features in interband transitions in the Faraday geometry are due to the transitions within the T ladder system, \mathbf{B} parallel to the valley axis. All valleys with their main axis oriented obliquely to \mathbf{B} exhibit a large number of interband transitions which more or less merge into one another and thus contribute to the enhanced background absorption. An unambiguous assignment to transitions within the L ladder system is therefore difficult and only possible for two or three absorption lines.

2. Voigt geometry

The experiments in the Voigt geometry yield information complementary to those in the Faraday geometry. Figure 12 shows experimental recordings of the transmission as a function of B for temperatures above and below T_c for $\text{Pb}_{1-x}\text{Ge}_x\text{Te}$, $x=0.01$. In both configurations $\mathbf{B} \parallel \mathbf{E}$ and $\mathbf{B} \perp \mathbf{E}$, $\mathbf{B} \parallel [1\bar{1}0]$, below T_c the modulation of transmission due to interband transitions is much less than above T_c . Such data were obtained for about 12 different CO-laser photon energies as a function of T .

In Figs. 13(a) and 13(b) fan charts for $T=45$ K (cubic phase) are presented for $\mathbf{E} \parallel \mathbf{B}$ and $\mathbf{E} \perp \mathbf{B}$ configurations. For $\mathbf{B} \parallel [1\bar{1}0]$ there are two sets of valleys oriented with their main axes, either with an angle of 35° or with 90° with respect to \mathbf{B} . For $\mathbf{E} \perp \mathbf{B}$ the selection rules are $n\alpha \rightarrow n\beta$ and $n\beta \rightarrow n\alpha$, whereas for $\mathbf{E} \parallel \mathbf{B}$, $n\alpha \rightarrow n\alpha$ and $n\beta \rightarrow n\beta$. For the 35° valleys in the $\mathbf{E} \parallel \mathbf{B}$ case, there is an

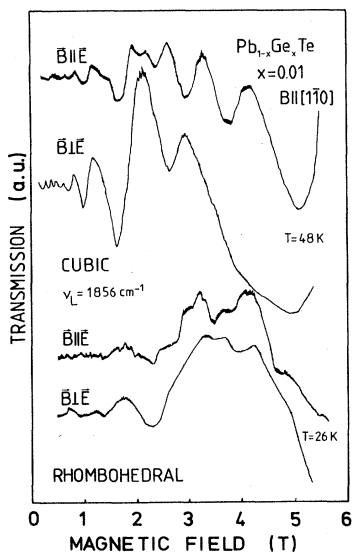


FIG. 12. Magneto-optical interband transmission vs magnetic field for two temperatures in the Voigt configuration, $\mathbf{B} \parallel [1\bar{1}0]$.

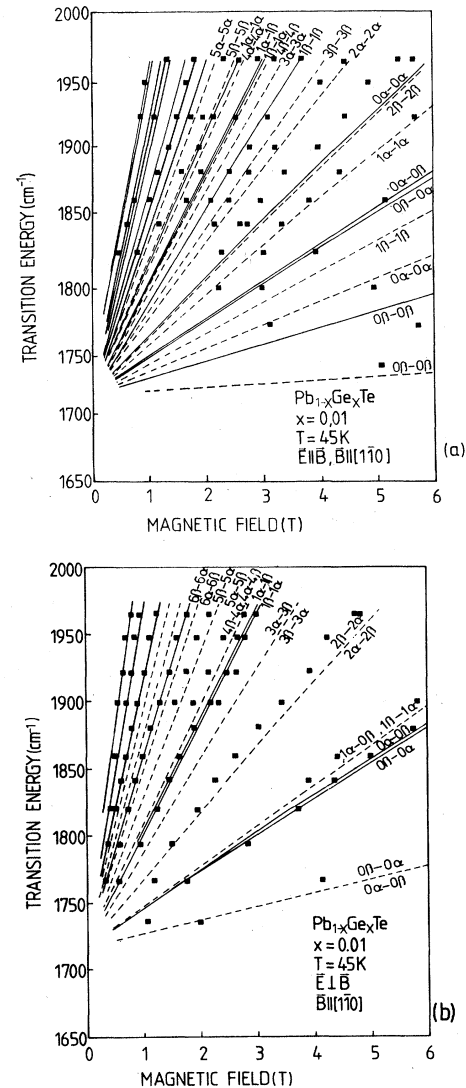


FIG. 13. Fan chart for transition energies vs B , Voigt configuration, $\mathbf{B} \parallel [1\bar{1}0]$. Experimental data: \blacksquare , calculated transition energies: solid lines, transitions involving Landau ladders in valleys oriented at $\approx 35^\circ$ with respect to \mathbf{B} ; dashed lines, corresponding transitions for valleys oriented at 90° with respect to \mathbf{B} . (a) Cubic phase ($T=45$ K), $\mathbf{E} \parallel \mathbf{B}$; (b) cubic phase ($T=45$ K), $\mathbf{E} \perp \mathbf{B}$.

additional transition series $n\alpha \rightarrow n\beta$ and $n\beta \rightarrow n\alpha$ of comparable oscillator strength. Whereas in the $\mathbf{E} \parallel \mathbf{B}$ configuration the interband transitions involving the 90° valleys dominate due to their higher transition matrix elements by a factor of 5, in the $\mathbf{E} \perp \mathbf{B}$ configuration the corresponding transitions involving the 35° and 90° valleys are of nearly equal strength. Despite the fact that CO-laser lines with small spectral width were used, the large number of possible transitions makes it difficult already in the cubic phase to find all transition minima in the $\mathbf{E} \parallel \mathbf{B}$ configuration. Closely lying minima merge into one another.

Figures 14(a) and 14(b) show the corresponding fan charts for the rhombohedral phase in the Voigt geometry for $T=31$ K. For $T < T_c$ the ratio of the transition ma-

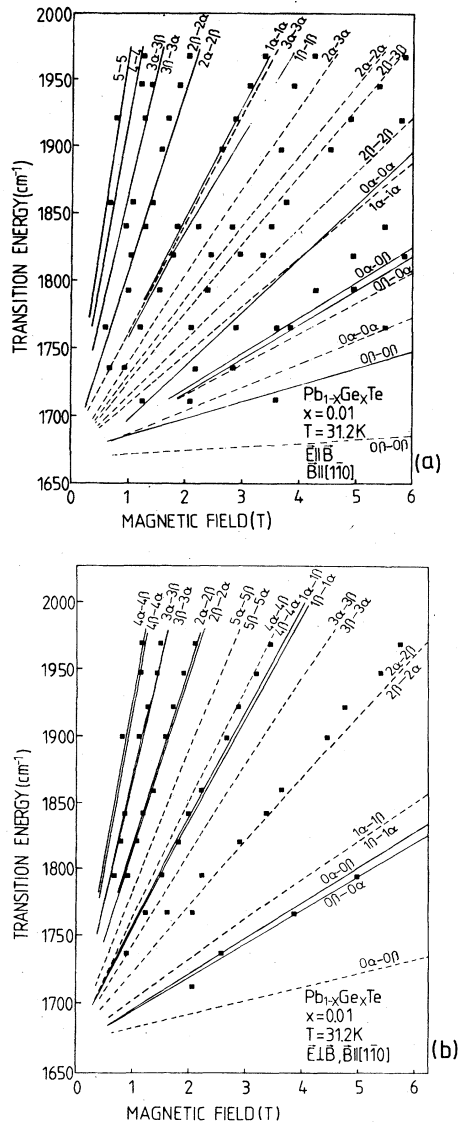


FIG. 14. Same as Fig. 13, but in the rhombohedral phase; calculated transitions for parameter $S = 4.8 \times 10^{-9}$ eV cm. (a) $T = 31.2$ K, $\mathbf{E} \parallel \mathbf{B}$; (b) $T = 31.2$ K, $\mathbf{E} \perp \mathbf{B}$.

trix elements for 90° and 35° valleys in the $\mathbf{E} \parallel \mathbf{B}$ configuration remain approximately the same as in the cubic phase. In the $\mathbf{E} \perp \mathbf{B}$ configuration the transitions involving the 35° valleys have substantially smaller matrix elements than in the cubic phase. As in the Faraday configuration, additional transitions become allowed below T_c , increasing the overall background absorption.

B. Intraband transitions

Magneto-optical intraband transitions were studied with different far-infrared laser photon energies for temperatures above and below the phase transition. In the cubic phase, for $\mathbf{B} \parallel [111]$, just two main structures due to cyclotron resonance in the valley oriented parallel to the surface normal and in the remaining three obliquely

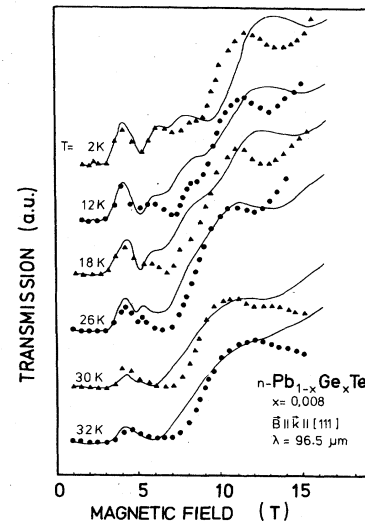


FIG. 15. Far-infrared laser transmission ($\lambda = 96.5$ μm) as a function of magnetic field for sample 112.3 in the Faraday configuration with temperature as the parameter. Lines, experimental results; \bullet and \blacktriangle , calculated transmission according to the formalism described in Sec. II. Parameter $S = 0$ (32 K), 1.2×10^{-9} (30 K), 2.4×10^{-9} (26 K), 3.6×10^{-9} (18 K), and 4.8×10^{-9} (12 and 2 K) (in units of eV cm). The free-carrier damping parameter is changed slightly with T . The T, L' levels are shifted downwards in energy relative to the L, L'', T' levels by 3 meV (4 meV for $T < 18$ K).

oriented valleys are expected. There is some difference in energy for the $0\alpha \rightarrow 1\alpha$ and $0\beta \rightarrow 1\beta$ transitions, which is, however, not resolved in $\text{Pb}_{1-x}\text{Ge}_x\text{Te}$ above T_c .

In Fig. 15 the transmission as a function of magnetic field is shown for sample 112.3 for a wavelength of 96.5 μm , with temperature as a parameter. The transition temperature T_c is about 32 K. Since the laser frequency lies between ω_{TO} and ω_{LO}^+ , the lattice real part of the dielectric function for this frequency is negative, and magneto-optical intraband transitions will manifest themselves as dielectric anomalies instead of transmission minima. Apparently, with decreasing temperature, more

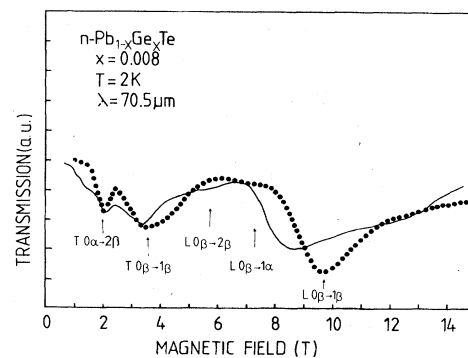


FIG. 16. Far-infrared laser transmission ($\lambda = 70.5$ μm) vs B (the photon energy is above the coupled phonon-plasmon frequency ω_{L}^+). Solid lines, experimental results; dots, calculated results for $S = 4.8 \times 10^{-9}$ eV cm. The magneto-optical transitions are indicated by arrows. T, L' -level shift as in Fig. 15.

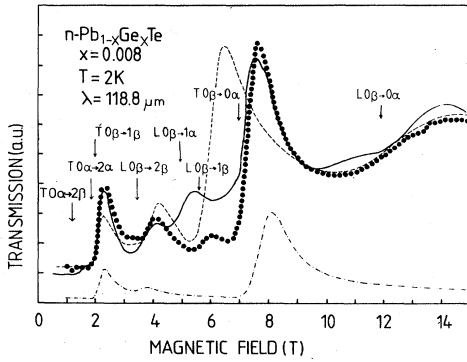


FIG. 17. Same as Fig. 16, but for $\lambda=118.8 \mu\text{m}$ (the photon frequency is below ω_L^+). Dots: calculated results with T, L' -level shifts as in Fig. 15. Dashed line: calculated results with T, L' levels not shifted with respect to the L, L'', T' levels (no deformation at all). Dashed-dotted line: calculated results with T, L' levels shifted by 15.5 meV [following Ferreira's (Ref. 55) deformation potentials], which corresponds, for this sample, to a situation wherein all carriers are within the T, L' valleys.

and more structures due to an increased number of magneto-optical transitions appear in the rhombohedral phase. Figures 16 and 17 show the dependence of transmission as a function of B for larger and smaller laser photon energies. For $\lambda=70.5 \mu\text{m}$, one has $\omega > \omega_L^+$ and thus the magneto-optical resonances are already associated with transmission minima. Figure 18 shows similar results for sample 77.4 ($x=0.01$).

However, the analysis of the data for $T < T_c$ is not straightforward. With decreasing temperature several effects occur: (i) The splitting in energy of the $n\alpha \rightarrow (n+1)\alpha$ and $n\beta \rightarrow (n+1)\beta$ cyclotron resonance transitions increases, both in the T as well as L valleys. (ii) Transitions forbidden in the cubic phase, such as combined spin-flip resonances ($0\beta \rightarrow 1\alpha$), spin-flip transitions ($0\beta \rightarrow 0\alpha$), and even cyclotron resonance harmonics ($0\alpha \rightarrow 2\alpha$) become allowed. Despite the fact that the matrix elements of these transitions are generally smaller than those for usual transitions, the oscillator strength also depends on the position of the Fermi level with respect to the initial and final states. The latter deter-

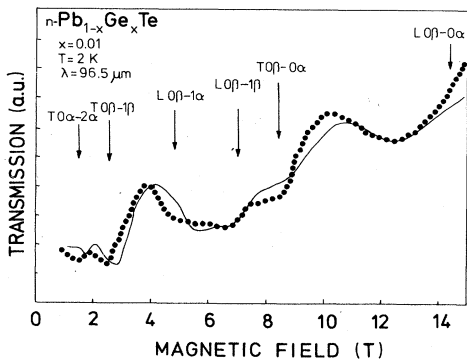


FIG. 18. Same as Fig. 16, but for sample 77.4 and $\lambda=96.5 \mu\text{m}$.

mines the number of carriers contributing to a given resonance. In Figs. 15–18 fits to the transmission spectra are shown, based on the treatment described in Sec. II. The various transitions are indicated by arrows and are identified. It turned out that it was necessary to shift the conduction-band edge of the T and L' valleys (A and B domains) in energy with respect to the L and L'' , and T' valleys in order to explain even the gross features of the spectra. If no such shift was assumed, the calculated transmission, as also shown in Fig. 17, does not agree at all with the experimental observed data. The calculated enhanced transmission due to the dielectric anomalies associated with the transverse mass resonance in the T and L' valleys turns out to be too small and the overall fit is much poorer. The origin of these shifts is the elastic deformation of the semiconductor film as discussed in Sec. V (see Fig. 23). With this shift, the variation of the Fermi level with B was calculated as shown in Fig. 19 for a temperature $T=2 \text{ K}$. The fits are based on the Landau levels also shown in Fig. 19, the linear-response formalism described in Sec. II, and the values for the phonon part in the dielectric function, where the stiffening of ω_{TO} with decreasing T below T_c is taken into account (see Table I).

From the dependence of the transition matrix elements on B , as given in Figs. 8(a) and 8(b), it is evident that with level crossings several transitions change their character. In Fig. 17, e.g., it appears that the $L_{0\beta} \rightarrow 1\beta$ and $L_{0\beta} \rightarrow 2\beta$ transitions are of comparable oscillator strength, whereas in Fig. 8(b) the dipole moments seem to be quite different. It must be indicated that the assignments given in Figs. 8(a) and 8(b) correspond to high magnetic fields. For example, at $B \approx 3.5 \text{ T}$, where for $\lambda=118.8 \mu\text{m}$ the cyclotron resonance harmonic transition $L_{0\beta} \rightarrow 2\beta$ is assigned in Fig. 17, the corresponding dipole moment, however, is given by the curve labeled $L_{0\beta} \rightarrow 1\alpha$ in Fig. 8(b), at higher magnetic fields. As evidenced by the kinks in $\hbar^2 d^2$ versus magnetic field, the final-state wave function changes its character from 2β to 1α toward higher fields. Thus for $B \approx 3.5 \text{ T}$, $\hbar^2 d^2$ for $L_{0\beta} \rightarrow 2\beta$ is approximately $0.2 \times 10^{-8} (\text{eV cm})^2$, whereas for the cyclotron transition $L_{0\beta} \rightarrow 1\beta$ at $B \approx 5.5 \text{ T}$ [cf. Figs. 17 and

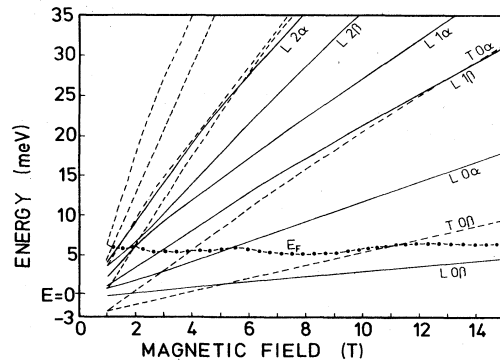


FIG. 19. Calculated Landau levels (T , dashed lines; L , solid lines) vs magnetic field. The T level is shifted downward by 3 meV with respect to the L levels. The variation of the Fermi energy ($T=2 \text{ K}$) with magnetic field is shown for sample 77.4 ($n=1.8 \times 10^{17} \text{ cm}^{-3}$); $S=6 \times 10^{-9} \text{ eV cm}$.

8(b)] this quantity is about 0.4×10^{-8} (eV cm)².

In magnetic field regions where the states change their character, the labels like $L2\beta$ are not a complete description of the wave functions. Thus transitions in these magnetic field regions cannot unambiguously be assigned as cyclotron resonance, cyclotron resonance harmonics, combined resonances, or spin-flip transitions in the sense of the usual terminology.

The variation of the transmission spectra with temperature is caused by the T dependence of the band parameters in the Landau-level calculation, namely E_G and S , and the consistent calculation of the variation of $E_F(B)$ necessary for elucidating the various magneto-optical transitions.

It is important to note that the calculated transmission spectra shown in Figs. 15–18 for samples 112.3 and 77.4 were aimed at yielding values for the k -linear parameter S . The “cubic” band parameters were kept constant in all fits, since the two- and far-band contributions were assumed not to vary for Ge contents between 0.8 and 1 at.%. The temperature dependence of the energy gaps was directly obtained from the magneto-optical interband measurements. Since the transmission in the far-infrared region critically depends on the carrier concentration n , n was determined for both samples by T -dependent Hall measurements. The lattice contribution to the frequency-dependent dielectric function was determined also independently by an analysis of reflectivity measurements.⁴⁵ The sample thicknesses were measured directly during the growth process and controlled by interference fringes in the near-infrared region.

Thus, apart from the electron damping parameter, only the k -linear parameter could be adjusted to obtain fits to the experimental recordings. In addition, the numerical value of S and its temperature dependence have to agree with that of the corresponding values deduced from the magneto-optical interband results. These conditions for the range of different S values are rather stringent, and together with the fixed values of all other parameters, are certainly not favorable for obtaining optimum fits to the magneto-optical intraband data.

V. DISCUSSION

A. Band parameters

The results of the magneto-optical interband and intraband transitions were fitted with model calculations as described in Secs. II and IV. The main aim was to obtain a consistent set of band parameters for a given temperature. The parameters which fit the cubic interband and intraband results in the cubic 4×4 Hamiltonian were kept constant, apart from minor variations of E_G with T . Below T_c , the temperature dependence results mainly from the rhombohedral parameter S in the $\mathbf{k} \cdot \mathbf{p}$ matrix. The fits to the experimental data were not aimed to be perfect for a single experimental curve, but for a consistent interpretation of interband and intraband data with the same parameter set for a given temperature. With the simplifying assumptions as discussed in Sec. II, the effects of the rhombohedral distortion are described alone by the

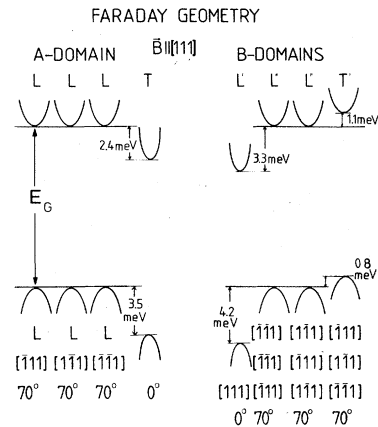


FIG. 20. Schematic diagram indicating the conduction- and valence-band extrema in one A and three B domains (Faraday geometry) with relative shifts in the energy consistent with the magneto-optical data, calculated by taking into account substrate-induced and phase-transition-induced strain, also including the deformation caused by the sublattice shift.

temperature dependence of the parameter S and by the changing E_G at T and L points of the BZ.

The relative positions of the corresponding extrema of the conduction and valence bands at the T , L , T' , and L'' points as shown in Fig. 20 are consistent with the experiments in Faraday geometry (see also Sec. VB). There are one A and three equivalent domains of B type. The relative shifts of the energy levels are necessary for the interpretation of the intraband magneto-optical transitions and agree with the results of the interband magnetoabsorption. In the Voigt configuration, for $\mathbf{B} \parallel [1\bar{1}0]$, there are three types of domains as shown in Fig. 21. The symbols have the same meaning as in Fig. 20. There are two domains of B type and one each of A and C type. The energy gaps at T and L' points are slightly different from each other and both are larger than the gaps at L and L'' points and T' points by about 1 meV (for $T=2$ K and $x=0.01$). The curvature in $E(\mathbf{k})$ indicates schematically the different cyclotron masses for the $\mathbf{B} \parallel [111]$ and $\mathbf{B} \parallel [1\bar{1}0]$ orientations, respectively, in Figs. 20 and 21.

The main result of the fits to the data is shown in Fig. 22, where the rhombohedral parameter S as a function of

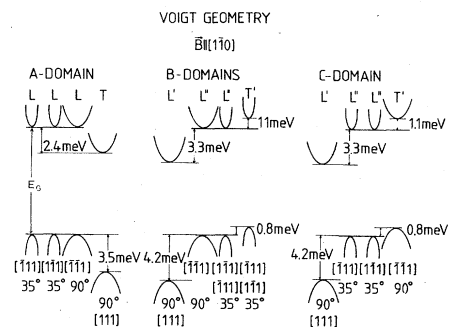


FIG. 21. Same as Fig. 20, but for Voigt geometry for one A , two B , and one C domain.

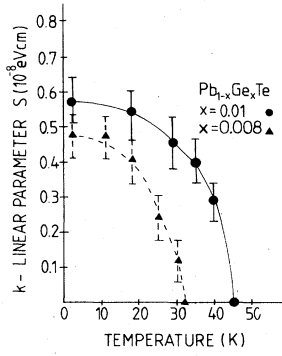


FIG. 22. Rhombohedral parameter S as a function of temperature for two $\text{Pb}_{1-x}\text{Ge}_x\text{Te}$ samples: ●, $x=0.01$; ▲, $x=0.008$.

temperature is given. All band parameters are listed in Table I, with the notation as introduced in Sec. II.

We would like to stress that in Sec. II, apart from the band parameter S , the rhombohedral distortion for the L valleys is described by one additional parameter R , for example. In the actual analysis this parameter was neglected, i.e., L and T valleys were treated equally. This simplification of the band theory is justified by expedience for the samples of interest. The relatively low Ge content and the energy gap of about 200 meV are the reasons that the rhombohedral distortion causes rather small energy shifts. Even for a band parameter R comparable to S , no further magneto-optical transitions would be observed within the L valleys, apart from those which are already introduced by the parameter S only. Therefore the conclusions as shown in Fig. 22 are certainly correct.

Concerning the magneto-optical transitions, the additional parameter R might alter the resonance positions due to the L valleys by small amounts. However, for our Ge concentrations the data would not allow a reasonable determination of a second k -linear parameter. For higher Ge concentrations ($x > 0.05$), where such a determination of two independent k -linear parameters might be possible, the reduction in mobility and thus scattering time broadens all magneto-optical transitions and prevents such a procedure.

B. Deformation potential

The rhombohedral distortion in $\text{Pb}_{1-x}\text{Ge}_x\text{Te}$ below T_C can be described in terms of three components: (i) a shift \mathbf{u} of the two sublattices relative to each other along that [111] direction which becomes the rhombohedral c axis, (ii) a shear component which manifests itself in a change $\Delta\alpha$ of the interaxial angle of the unit cell (see Fig. 1), and (iii) a change Δa of the lattice constant.^{45,49}

Dynamically, the relative sublattice shift corresponds to an optical-type deformation. As was shown in Sec. II, the effect of the rhombohedral distortion for the T point of the BZ is described by a single parameter Δ_1^T as defined in Eq. (2). However, Δ_1^T has the form of an interband optical deformation potential d_T as, e.g., defined in Ref. 50:

$$\langle \psi_{v,k}(\mathbf{r}) | \delta H | \psi_{c,k}(\mathbf{r}) \rangle = \frac{|\mathbf{u}|}{2a} d_T, \quad (29)$$

where $\psi_{v,k}$ and $\psi_{c,k}$ are valence- and conduction-band states, and δH represents the change of the Hamiltonian due to an optical-type deformation, in our case $\mathbf{u}=(a/2)(\delta,\delta,\delta)$.

With the definition of Δ_1^T in Eq. (2), Eq. (29) is equivalent to it and Δ_1^T is given by

$$(\Delta_1^T)^2 = (d_T/2)^2 (\mathbf{u}/a)^2. \quad (30)$$

On the other hand, Δ_1^T is related to the k -linear parameter S from Eq. (11):

$$S = L \sin(2\theta) = 2L \Delta_1^T / [E_G^2 + (2\Delta_1^T)^2]^{1/2}.$$

Using $E_G(\text{cubic})=0.190$ eV, $S=6 \times 10^{-9}$ eV cm, $L=4.3 \times 10^{-8}$ eV cm, and $\Delta_1^T=13.4$ meV results. Since the optical deformation potential is of interest by itself, we have estimated $|\mathbf{u}|(T)$ for $x=0.01$ from the data of $\Delta\alpha(T)$ given in Ref. 11 and the relation $u^2=\Delta\alpha/\eta$. Using $\eta=55$ deg/ \AA^2 according to Ref. 45 and $\Delta\alpha=2\epsilon_s$ (shear strain due to the phase transition: $\epsilon_s=0.16 \times 10^{-3}$ for $x=0.01$ causes a change of the interaxial angle $\Delta\alpha=1.1^\circ$), $|\mathbf{u}|=1.83 \times 10^{-2}$ \AA results. With a lattice constant $a=6.43$ \AA and the value of $\Delta_1^T=13.4$ meV, Eq. (33) gives $d_T=10$ eV for the optical deformation potential.

This method of evaluating the optical interband deformation potential of $\text{Pb}_{1-x}\text{Ge}_x\text{Te}$ from magneto-optical data is certainly the most direct one used so far. Previously, d_T was estimated from the T dependence of the energy gap and from an elaborate interpolation of the resistance anomaly.^{23,27}

Recently, Vogl and Kocevar⁵¹ have performed band-structure calculations for various IV-VI compounds using the LCAO method. In order to obtain an expression for the optical interband deformation potential, they calculated the change of the overlap integrals induced by the optical deformation according to the dependence of $V_{pp\sigma}$ and $V_{pp\pi}$ on $1/r^2$, r denoting the distance between anion and cation.⁵² For PbTe and a distortion along the [111] direction, a value of 16 eV was obtained.⁵³ The agreement between the value of 10 eV derived from our experiments⁴⁵ and this completely independent LCAO calculation of d_T is reasonable.⁵⁴

At the L point of the BZ the rhombohedral distortion induces two different interband matrix elements as given in Eq. (2). The first is equivalent to that of the T point, mixing α and α or β and β states of L_6^- and L_6^+ . The second mixes α and β states, or β and α states, respectively. The optical deformation causes a change of the energy gap since the squares of these matrix elements enter in the expression for the rhombohedral gap, as shown in Eq. (8).

For the above-defined distortion \mathbf{u} , the LCAO calculation leads to a value for the optical deformation potential of 12 eV for the L point, in comparison to 16 eV for the T point of the BZ. In principle, these differences should be observable in the temperature dependence of the gaps at T and L points in the rhombohedral phase. However, the values of the rhombohedral gaps are not only determined by the optical-type deformation, but also by the shear and dilatational components. Thus, as already shown in Eq. (3), acoustic deformation potentials enter into the gap values [Eq. (8)].

Values of acoustic deformation potentials were published by Ferreira⁵⁵ for PbTe. Thus, in principle, with Ferreira's values the dilatation- and shear-induced change of the energy gap could be found. However, we have some evidence that the values for D_u and D_d given by Ferreira are too large. In our epitaxial films there is, in addition, substrate-induced strain which lifts the degeneracy of the four valleys already in the cubic phase and changes their gaps with respect to the bulk material.^{56,57} The influence of strain has been determined by x-ray measurements as a function of temperature between 300 and 40 K for $\text{Pb}_{0.99}\text{Ge}_{0.01}\text{Te}$. From measurements of different x-ray-diffraction peaks of lattice planes parallel and inclined to the sample surface normal, the tensor components of ϵ_{ij} were determined. Resulting values for $\epsilon_{ij}=\epsilon_d$ are 3×10^{-4} and $\epsilon_{ij}=\epsilon_s$ are -7×10^{-4} ($T=40$ K). The energy shifts are then given by

$$\delta E_{c,v}^{[111]} = (3D_d^{c,v} + D_u^{c,v})\epsilon_d + 2D_u^{c,v}\epsilon_s, \quad (31)$$

$$\delta E_{c,v}^{\langle\bar{1}\bar{1}\bar{1}\rangle} = (3D_d^{c,v} + D_u^{c,v})\epsilon_d - \frac{2}{3}D_u^{c,v}\epsilon_s. \quad (32)$$

Using Ferreira's values, large changes of the various [111] and $\langle\bar{1}\bar{1}\bar{1}\rangle$ conduction and valence levels result. From the experimentally observed energy shifts, it seems that the deformation potentials D_d and D_u are—by about a factor of 4—smaller than those given in Ref. 55.

In Fig. 23 the energy levels and the influence of the three different contributions are schematically shown. In the cubic films grown on BaF_2 [111] substrates, the [111] and $\langle\bar{1}\bar{1}\bar{1}\rangle$ levels are split by substrate-induced strain: the [111] levels are shifted downwards in energy in both the conduction and valence bands by 3 and 4 meV, respectively

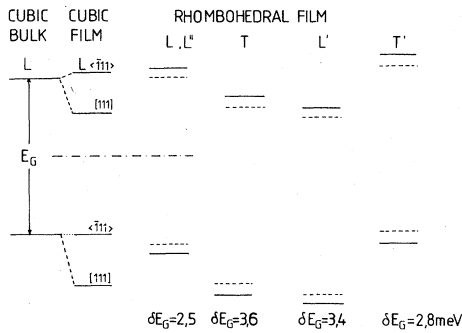


FIG. 23. Schematic representation of various contributions to the band-gap shifts in $\text{Pb}_{1-x}\text{Ge}_x\text{Te}$ ($x=0.01$, $T=1.6$ K). In cubic films on BaF_2 (111) substrates, the substrate-induced strain lifts the degeneracy of the four equivalent L extrema: The [111] valley oriented parallel to the surface normal is shifted downwards in the conduction as well as the valence band. Below the phase-transition temperature, the deformation of the elementary cell characterized by $\Delta\alpha$ [δ_i^p , see Eq. (21)] leads to the energy levels indicated by the dashed lines for the T , L' , L , and (L'' , T') points of the BZ (points in angular brackets correspond to domains with c' axes oblique to the surface normal). The solid lines (rhomboidal film) correspond to the additional enlargement of the gaps due to the optical-type deformation, characterized quantitatively by $\Delta_1^{T,L}$ [see Eq. (24)]. Energy shifts are drawn to scale, apart from E_G .

ly [using Eqs. (31) and (32) and measured values for ϵ_d and ϵ_s]. The energy gaps at [111] and $\langle\bar{1}\bar{1}\bar{1}\rangle$ L points change only slightly.

Below T_c the dilatation- and shear-induced changes of the energy gaps at the T , L'' , L' and T' points (in the notation of Fig. 6) are indicated for $T=1.6$ K, where the starting levels are those of the cubic $\text{Pb}_{1-x}\text{Ge}_x\text{Te}$ films. For $x=0.01$ the rhombohedral shear and dilatation strain tensor components are $\epsilon_2=1.6 \times 10^{-4}$ and $\epsilon_d=1.7 \times 10^{-4}$. In order to calculate the corresponding shifts of the energy levels due to this rhombohedral unit-cell distortion, Eq. (31) can be used to obtain δ^T and Eq. (32) for δ^L . These shifts are shown in Fig. 23 for the T , L' , L and L'' extrema by the dashed lines. The third contribution, the optical deformation, symmetrically increases the various gaps according to Eq. (8) [as shown in Fig. 23 by the solid lines based on $\Delta_1^T=13.4$ meV and Eq. (8)]. With our choice of the intraband deformation potentials and optical deformation potentials, the gaps at T and L' points are comparable to each other and both are about 1 meV larger than those at the L and L'' , and T' points. Owing to the rhombohedral shear-, dilatation-, and optical-deformation-induced shifts, the relative position of the T , L , L' , L'' , and T' levels changes, but the main difference between T , L' , and all the other levels is still caused by the substrate-induced strain for samples with Ge contents < 1 at. %.

The relative positions of the various levels were originally obtained from the fits to the magneto-optical intraband data. They are compatible with the interband data. The consistent description of the experimental data is possible only with the level shifts, including those obtained from acoustic deformation potentials, if the Ferreira values $D_u^{c,v}$ and $D_d^{c,v}$ are reduced by a factor of about 4. The optical deformation potential is in agreement with the value obtained from the LCAO calculation within a factor of 2.

VI. CONCLUSION

The influence of the structural phase transition in the pseudobinary $\text{Pb}_{1-x}\text{Ge}_x\text{Te}$ system on the electronic band-edge structure was investigated theoretically and experimentally. The effect of the reduced symmetry in the rhombohedral phase on the energy-momentum relationship of the free carriers was studied by use of the $\mathbf{k}\cdot\mathbf{p}$ method. Landau levels were calculated and the allowed electric dipole transitions were obtained for interband as well as for intraband magneto-optics. These results were applied to experimentally observed magneto-optical transitions in the near infrared (band-to-band transitions), as well as in the far-infrared region.

It was shown that with justified assumptions for low Ge content (L and T valleys treated similarly) the effect of the rhombohedral distortion is properly accounted for by introducing one additional matrix element in the $\mathbf{k}\cdot\mathbf{p}$ Hamiltonian to the cubic ones. This additional matrix element has a temperature dependence due to the second-order-type phase transition (O_h-C_{3v}) and establishes a secondary order parameter.

For a given temperature and composition, it was possi-

ble to describe both intraband and interband magneto-optical data with one set of band parameters. The additional "rhombohedral" parameter S causes the appearance of k -linear terms in the $E(k)$ relationship and removes the Kramers degeneracy at the T and L points of the BZ.

By relating the primary order parameter u , the sublattice shift, to an optical deformation potential at the T and L points, it was possible to determine these optical deformation potentials from a comparison of experiments with calculations. The resulting values are in reasonable agreement with predictions of a recent LCAO calculation of deformation potentials. Information on acoustic deforma-

tion potentials was obtained from strain measurements using x-ray techniques.

ACKNOWLEDGMENTS

This work was supported by Fonds zur Förderung der wissenschaftlichen Forschung, under Project Nos. P3044 and P4045, Austria. The samples used in the present investigations were grown by Professor A. Lopez-Otero. The far-infrared magneto-optical experiments in fields up to 18 T were carried out at the High Magnetic Field facility of the Max-Planck-Gesellschaft, Grenoble, with the aid of Professor M. von Ortenberg, who contributed helpful discussions as well.

*Present address: Physikalisches Institut der Universität Bayreuth, D-8580 Bayreuth, Federal Republic of Germany.

¹R. Dalven, in *Solid State Physics*, edited by H. Ehrenreich, F. Seitz, and D. Turnbull (Academic, New York, 1973), Vol. 28, p. 179.

²Yu. I. Ravich, B. A. Efimova, and I. A. Smirnow, *Semiconducting Lead Chalcogenides* (Plenum, New York, 1970).

³*Physics of IV-VI Compounds and Alloys*, edited by S. Rabii (Gordon and Breach, London, 1974).

⁴R. S. Allgaier, *Proc. SPIE* **285**, 2 (1981).

⁵E. Burstein, A. Pinczuk, and R. F. Wallis, in *The Physics of Semimetals and Narrow Gap Semiconductors*, edited by D. L. Carter and R. T. Bate (Pergamon, New York, 1971), p. 251.

⁶G. Bauer, in *Narrow Gap Semiconductors, Physics and Applications*, Vol. 133 of *Lecture Notes in Physics*, edited by W. Zawadzki (Springer, Berlin, 1980), p. 407.

⁷W. Jantsch, *Dynamical Properties of IV-VI Compounds*, Vol. 99 of *Springer Tracts in Modern Physics*, edited by G. Höhler (Springer, Berlin, 1983), p. 1.

⁸H. Kawamura, in *Narrow Gap Semiconductors, Physics and Applications*, Ref. 6, p. 470.

⁹K. Murase, in *Proceedings of the 15th International Conference on the Physics of Semiconductors, Kyoto, 1980* [J. Phys. Soc. Jpn. Suppl. A **49**, 725 (1980)].

¹⁰G. S. Pawley, W. Cochran, R. A. Cowley, and G. Dolling, *Phys. Rev. Lett.* **17**, 759 (1966).

¹¹D. K. Hohnke, H. Holloway, and S. Kaiser, *J. Phys. Chem. Solids* **33**, 2053 (1972).

¹²R. Clarke, *Phys. Rev. B* **18**, 4290 (1978).

¹³M. E. Lines and A. M. Glass, *Principles and Applications of Ferroelectrics and Related Materials* (Clarendon, Oxford, 1977).

¹⁴K. Schubert and H. Fricke, *Z. Naturforsch.* **6a**, 781 (1951).

¹⁵W. Cochran, R. A. Cowley, G. Dolling, and M. M. Elcombe, *Proc. R. Soc. London, Ser. A* **293**, 433 (1966).

¹⁶E. F. Steigmeier and G. Harbecke, *Solid State Commun.* **8**, 1275 (1970).

¹⁷K. Murase and S. Sugai, *Solid State Commun.* **32**, 89 (1979).

¹⁸G. Bauer, H. Burkhard, W. Jantsch, F. Unterleitner, A. Lopez-Otero, and G. Schlessner, in *Proceedings of the International Conference on Lattice Dynamics*, edited by M. Balkanski (Flammarion, Paris, 1977), p. 669.

¹⁹W. Jantsch, G. Bauer, and A. Lopez-Otero, *Infrared Phys.* **18**, 877 (1978); in *Proceedings of the 14th International Conference on the Physics of Semiconductors*, edited by B. L. H. Wilson (Institute of Physics, London, 1978), p. 445.

²⁰S. Sugai, K. Murase, T. Tsuchihara, and H. Kawamura, *J. Phys. Soc. Jpn.* **47**, 539 (1979).

²¹R. T. Bate, D. L. Carter, and J. S. Wrobel, *Phys. Rev. Lett.* **29**, 159 (1970).

²²W. Jantsch and A. Lopez-Otero, in *Proceedings of the 13th International Conference on the Physics of Semiconductors*, edited by F. G. Fumi (Tipografia Marves, Rome, 1976), p. 487.

²³S. Takaoka and K. Murase, *Phys. Rev. B* **20**, 2823 (1979); T. Suski, S. Takaoka, K. Murase, and S. Porowski, *Solid State Commun.* **45**, 259 (1983); S. Katayama and D. L. Mills, *Phys. Rev. B* **22**, 336 (1980).

²⁴J. R. Burke, B. B. Houston, H. T. Savage, J. Babiskin, and P. G. Siebenmann, *J. Phys. Soc. Jpn.* **21**, 384 (1966); H. T. Savage, B. B. Houston, and J. R. Burke, *Phys. Rev. B* **6**, 2292 (1972).

²⁵Y. He and A. D. C. Grassie, in *Application of High Magnetic Fields in Semiconductor Physics*, Vol. 177 of *Lecture Notes in Physics*, edited by G. Landwehr (Springer, Berlin, 1983), p. 369; Ferroelectrics (to be published); *Phys. Rev. B* **30**, 2937 (1984).

²⁶W. Jantsch, *Z. Phys. B* **40**, 193 (1980).

²⁷S. Takaoka and K. Murase, *J. Phys. Soc. Jpn.* **51**, 1857 (1982).

²⁸A. V. Lewis, R. J. Nicholas, J. C. Ramage, G. Bauer, A. Lopez-Otero, and R. A. Stradling, *J. Phys. C* **13**, 561 (1980); **13**, L443 (1980).

²⁹E. J. Fantner, H. Pascher, G. Bauer, R. Danzer, and A. Lopez-Otero, in *Proceedings of the 15th International Conference on the Physics of Semiconductors, Kyoto, 1980* [J. Phys. Soc. Jpn. Suppl. A **49**, 741 (1980)].

³⁰G. Bauer, in *Application of High Magnetic Fields in Semiconductor Physics*, Ref. 25, p. 259.

³¹D. L. Mitchell and R. F. Wallis, *Phys. Rev.* **151**, 581 (1966).

³²E. Bangert, in *Physics of Narrow Gap Semiconductors*, Vol. 152 of *Lecture Notes of Physics*, edited by E. Gornik (Springer, Berlin, 1982), p. 216.

³³W. Jantsch, G. Bauer, A. Krost, and A. Lopez-Otero, *Ferroelectrics* **38**, 905 (1981).

³⁴E. D. Palik, L. D. Mitchell, and J. N. Zemel, *Phys. Rev.* **135**, A763 (1964).

³⁵J. M. Luttinger, *Phys. Rev.* **102**, 1030 (1956).

³⁶H. R. Trebin, U. Roessler, and R. Ranvaud, *Phys. Rev. B* **20**, 686 (1979).

³⁷G. F. Koster, J. O. Dimmock, R. G. Wheeler, and H. Statz, *Properties of the 32 Point Groups* (MIT Press, Cambridge, Mass., 1963).

³⁸H. M. Polatoglou, G. Theodorou, and N. A. Economou, in *Physics of Narrow Gap Semiconductors*, Ref. 32, p. 221.

³⁹G. Martinez, M. Schlüter, and M. L. Cohen, *Phys. Rev. B* **11**, 651 (1975); **11**, 660 (1975); **11**, 3808 (1975).

⁴⁰M. S. Adler, C. R. Hewes, and S. D. Senturia, *Phys. Rev. B* **7**,

- 5186 (1973).
- ⁴¹H. Burkhard, G. Bauer, and A. Lopez-Otero, *J. Opt. Soc. Am* **67**, 946 (1977); *Solid State Commun.* **18**, 773 (1976).
- ⁴²P. R. Wallace, *Phys. Status Solidi* **38**, 715 (1970).
- ⁴³H. Burkhard, G. Bauer, and W. Zawadzki, *Phys. Rev. B* **19**, 5149 (1979).
- ⁴⁴S. W. McKnight and H. D. Drew, *Phys. Rev. B* **21**, 3447 (1980).
- ⁴⁵G. Bauer, W. Jantsch, and E. Bangert, in *Festkörperprobleme*, edited by P. Grosse (Pergamon/Vieweg, Braunschweig, 1983), Vol. XXIII, p. 27.
- ⁴⁶A. Lopez-Otero, *Thin Solid Films* **49**, 1 (1978).
- ⁴⁷G. Appold, R. Grisar, G. Bauer, H. Burkhard, R. Ebert, H. Pascher, and H. G. Haefele, in *Proceedings of the 14th International Conference on the Physics of Semiconductors*, Ref. 19, p. 1101.
- ⁴⁸G. Appold, Ph.D. thesis, University of Würzburg, 1979.
- ⁴⁹W. Jantsch, in *Physics of Narrow Gap Semiconductors*, Ref. 32, p. 221.
- ⁵⁰G. Vogl, in *Physics of Nonlinear Transport in Semiconductors*, edited by D. K. Ferry, J. R. Barker, and C. Jacoboni (Plenum, New York, 1980), p. 75.
- ⁵¹G. Vogl and P. Kocevar (unpublished).
- ⁵²W. A. Harrison, *Electronic Structure and the Properties of Solids* (Freeman, San Francisco, 1980).
- ⁵³M. Cardona and P. Vogl, *Ferroelectrics* (to be published).
- ⁵⁴The experimental and theoretical values of d_T given in Ref. 45, namely 20 and 32 eV, respectively, are in error by a factor of 2.
- ⁵⁵L. G. Ferreira, *Phys. Rev.* **137**, A1601 (1965).
- ⁵⁶J. R. Burke and G. P. Carver, *Phys. Rev. B* **19**, 402 (1979).
- ⁵⁷E. J. Fantner, H. Clemens, and G. Bauer, in *Advances in X-Ray Analysis*, edited by J. B. Cohen, J. C. Russ, D. E. Leyden, C. S. Barrett, and P. K. Predecki (Plenum, New York, 1984), Vol. 27, p. 171.